



Research papers

Transient tidal eddy motion in the western Gulf of Maine,
part 1: Primary structure

W.S. Brown*, G.M. Marques

School for Maine Science & Technology, University of Massachusetts Dartmouth, New Bedford, MA, United States

ARTICLE INFO

Article history:

Received 5 April 2011

Received in revised form

26 July 2012

Accepted 17 August 2012

Available online 8 September 2012

Keywords:

Coastal tidal eddy motion

Eddy motion kinematics

Tidal dynamics

Numerical tidal modeling

Current measurements

Western Gulf of Maine

ABSTRACT

High frequency radar-derived surface current maps of the Great South Channel (GSC) in the western Gulf of Maine in 2005 revealed clockwise (CW) and anticlockwise (ACW) eddy motion associated with the strong regional tidal currents. To better elucidate the kinematics and dynamics of these transient tidal eddy motions, an observational and modeling study was conducted during the weakly stratified conditions of winter 2008–2009. Our moored bottom pressure and ADCP current measurements in 13 m depth were augmented by historical current measurements in about 30 m in documenting the dominance of highly polarized M_2 semidiurnal currents in our nearshore study region. The high-resolution finite element coastal ocean model (QUODDY) – forced by the five principal tidal constituents – produced maps depicting the formation and evolution of the CW and ACW eddy motions that regularly follow maximum ebb and flood flows, respectively. Observation versus model current comparison required that the model bottom current drag coefficient be set to at an unusually high $C_d=0.01$ – suggesting the importance of form drag in the study region. The observations and model results were consistent in diagnosing CW or ACW eddy motions that (a) form nearshore in the coastal boundary layer (CBL) for about 3 h after the respective tidal current maxima and then (b) translate southeastward across the GSC along curved 50 m isobath at speeds of about 25 m/s. Observation-based and model-based momentum budget estimates were consistent in showing a first order forced semidiurnal standing tidal wave dynamics (like the adjacent Gulf of Maine) which was modulated by adverse pressure gradient/bottom stress forcing to generate the eddy motions. Observation-based estimates of terms in the transport vorticity budget showed that in the shallower Inner Zone subregion (average depth=23 m) that the diffusion of nearshore vorticity was dominant in feeding the growth of eddy motion vorticity; while in the somewhat deeper Outer Zone subregion (33 m) bottom current lateral shear and water column stretching/squashing was significant in modulating the eddy motion. We conclude that the transient eddy motions in the GSC region are phase eddies that accompany the change of tide across the GSC and are (1) generated by bottom stress gradients in the shallower nearshore – an issue which needs to be better understood for improved future forecasting.

© 2012 Elsevier Ltd. All rights reserved.

1. Introduction

Tide-induced eddy motions are found in many different coastal ocean regions featuring curved coastlines and promontories (Pingree, 1978; Pingree and Maddock, 1980; Black and Gay, 1987; Wolanski et al., 1996; Geyer and Signell, 1990). The observed eddies apparently are caused by different mechanisms – depending on local circumstances. In one Australian case, Black and Gay (1987) found that unsteadiness of flow at semidiurnal tidal frequencies is demonstrated to be a dominant factor forming eddies in their continental shelf environment. They used both field measurements and numerical hydrodynamic modeling to show that during the later stages of the half tidal cycle in a low-friction environment, currents in the lee of an

obstruction accelerate with supporting sea gradients opposite to the adjacent, inertial free stream, which is still decelerating. These opposed currents appear as what they call a phase eddy and ideally can endure for 3 h in reversing M_2 – S_2 tidal currents.

In another case of tidal eddies in Vineyard Sound, Massachusetts, Geyer and Signell (1990) observed flow separation and the formation of distinct transient eddies downstream of alternate sides of a headland during the flood and ebb tidal flows, respectively. They were able to show that through the course of either the flood (or ebb) flow, distinct eddies started out as a small concentrated patch of vorticity just behind the headland and grew into an elongated eddy as it translated downstream. The Signell and Geyer (1991) theoretical and numerical modeling results strongly suggest that coastal boundary layer separation physics lay at the heart of that observed transient tidal eddy generation process.

More recently, eddy motions have been detected in the hourly surface current maps that are produced from high frequency radar (HF radar; 5 MHz in this case) measurements by a pair of

* Correspondence to: School for Marine Science and Technology, University of Massachusetts Dartmouth, 706 S Rodney French Blvd., New Bedford, MA 02744-1221, United States. Tel.: +1 508 910 6395; fax: +1 508 910 6371.

E-mail address: wbrown@umassd.edu (W.S. Brown).

Coastal Ocean Dynamics Applications Radar (CODAR) installations; one near Nauset, MA and the other on Nantucket Island (see Fig. 1). Surface current maps of the region east of Cape Cod, MA from early April 2005 (Brown and Yu, 2006) suggest the formation of alternating clockwise (CW) and anticlockwise (ACW) eddy motions in association with respective ebb and flood tidal flows (see Fig. 1). Both of these eddy features translate south-eastward into the central Great South Channel (GSC) region of the western Gulf of Maine (GoM); and then disappear near the end of the ebb (or flood) flow phase. These HF radar-derived current observations are supported by realistic numerical tidal model simulations (see Brown and Yu, 2006), which also clearly reveal

the transient upwelling and downwelling secondary flows that are associated with both the primary and eddy motions.

Many of these studies report on the secondary flows associated with tide-induced eddy motions. For example, Geyer (1993) reports that secondary flow represents about 20% of the principal tide-induced eddy motions off of Gay Head, Martha's Vineyard Gay Head, Martha's Vineyard. However, there are indications that the dynamics of these eddy motions and their associated secondary flows differ. The persistent presence eddy motions and their associated downwelling and upwelling can be potentially important environmental factors for applications ranging from search and rescue forecasting to recruitment to the regional fisheries. More specifically, the details of

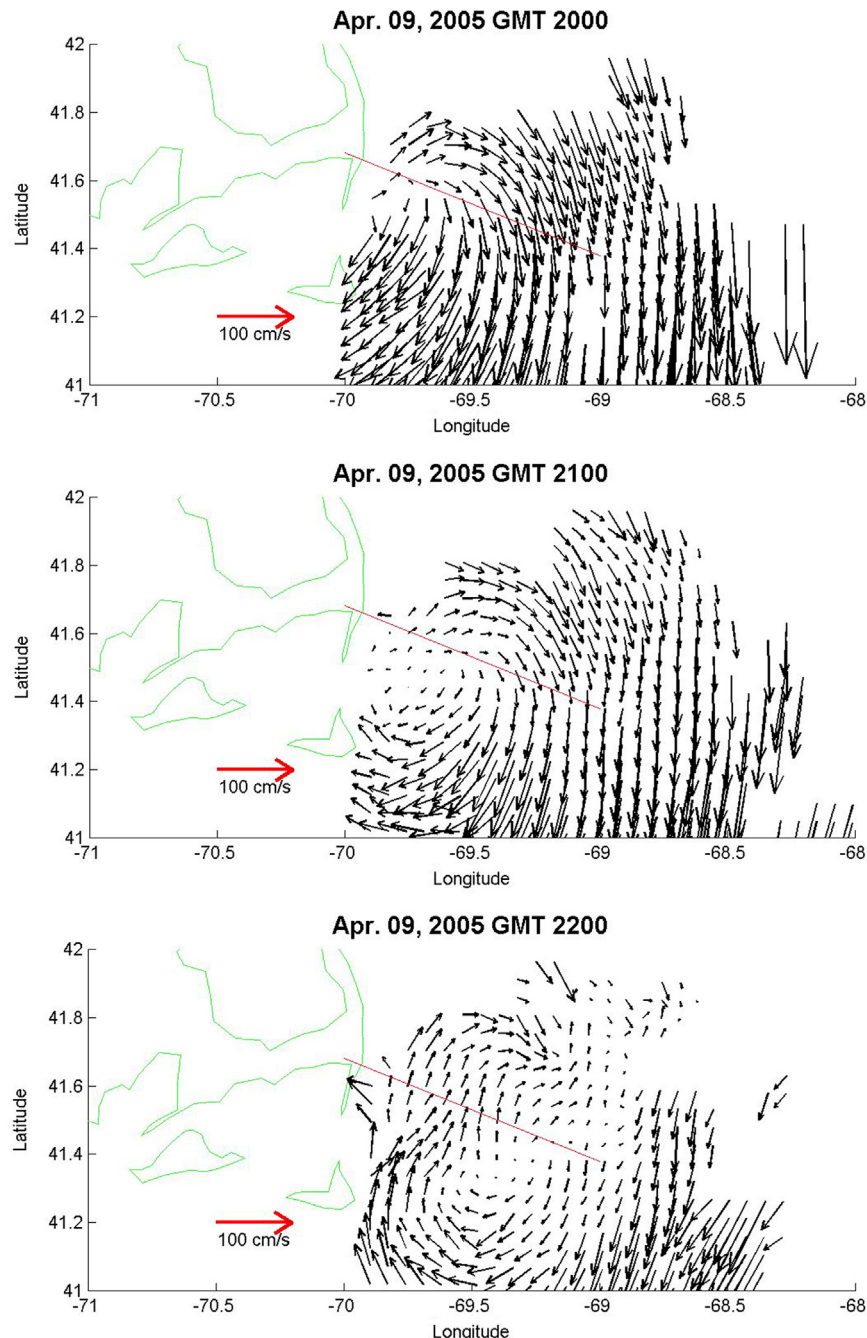


Fig. 1. A sequence of hourly maps of surface currents derived from high-frequency radar (CODAR) measurements at Nauset, MA and on Nantucket Island in the Great South Channel (GSC) east of the elbow of Cape Cod on 9 April 2005 showing evolving clockwise eddy motion (upper panel) originating near the coast at 2000 UTC; (middle panel) growing in scale at 2100 UTC; and (lower panel) filling the western GSC (after Brown and Yu, 2006).

this secondary flow environment may be important to the settlement of scallop larvae (i.e., spat) and/or the general maintenance of the local scallop fishery (Stokesbury et al., 2004).

To address questions regarding basic transient tidal eddy motion characteristics and mechanisms, we conducted a field observation/model study during the winter of 2008–2009 when the stratification was very weak. We have produced a pair of papers to describe the processes associated with this tidal eddy motion. In this paper, we describe the primary structure and dynamics of the tide-induced eddy motion; as inferred from the ocean observations and numerical ocean circulation model results. In the second paper, Marques and Brown (this issue, henceforth MB12), we describe the secondary flows associated with the primary tidal flow and modulated by the eddy motion.

This paper is organized as follows. The field measurements are described in Section 2. The numerical model and setup are described in Section 3. In Section 4, we present the basic observational time series results, model results in terms of a set of model surface current maps and observation/model comparisons. In Section 5, observation and model results are integrated in a description of the formation process of the tidal eddy motion. In Section 6, the eddy motion dynamics are explored in terms of estimates of the momentum and transport vorticity budgets. In Section 7, we discuss our interpretation of the results. In Section 8 there is a summary of our conclusions. Appendices contain relevant harmonic constants of our observations, and algorithms used to estimate terms in the momentum and vorticity transport budgets, respectively.

2. Observations

The field component of the study was conducted under winter conditions between 3 November 2008 and 28 January 2009 in the western Gulf of Maine in the Great South Channel just east of Chatham, MA (see Fig. 2; Table 1). High frequency (HF) radar-derived

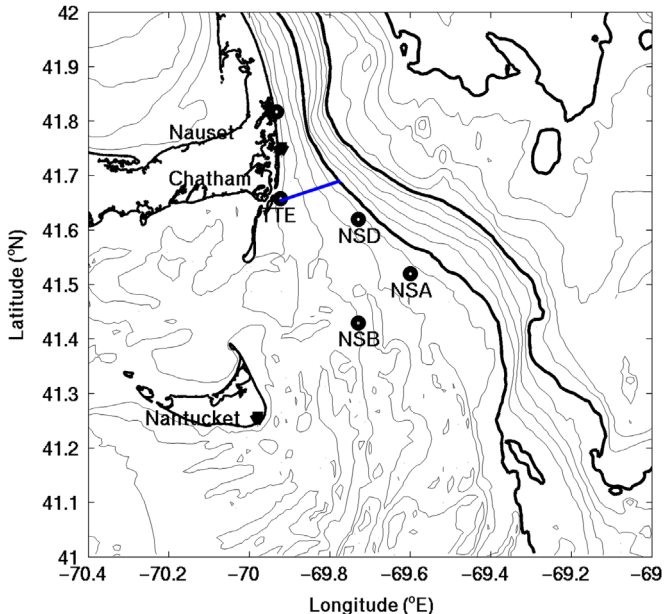


Fig. 2. The map of the study region just offshore from Chatham, MA in the western Great South Channel/Gulf of Maine. The study's moored current/bottom pressure station (TTE bold circle), HF radar stations at Nauset and Nantucket (inverted triangles), and hydrographic survey (line) transect are located; along with historical current stations (bold circles at NSA, NSB, and NSD), bottom pressure station (bold circle) off of Nauset, MA. The isobaths are given in 10 m intervals from the coast to 100 m; then 20 m intervals into deeper waters; with bolder 50 m, 100 m, and 200 m isobaths.

Table 1

Locations of the field program measurement stations (*italics*). Also shown are the locations of historic measurement stations for which we have tidal harmonic constants.

Station ID	Station longitude °W	Station latitude °N	Station depth (m)	Record depth (m)	Record length (days)
Bottom pressure					
TTE	69.923	41.658	13	12	58
Nauset	69.933	41.817	7	6	58
Moored currents					
TTE	69.923	41.658	13	6, 8	58
NSD	69.730	41.620	33	16	42
NSA	69.600	41.520	33	5, 25	60
NSB	69.730	41.430	23	10	42
HF radar currents					
<i>Nauset</i>	69.920	41.800	–	–	87
<i>Nantucket</i>	69.980	41.255	–	–	87

surface currents were constructed from radial currents that were measured from stations at Nauset and Nantucket Island, MA. Bottom-mounted current and pressure time series measurements were made at station TTE. A 27 January 2009 shipboard CTD water property survey was conducted.

Shipboard Hydrography: Hydrographic measurements showed that the water column was well mixed during the observation period. These measurements were obtained using an internally recording Seabird® SBE-25 Sea-logger to measure conductivity (C) and temperature (T) versus pressure (P) profiles during a 7-station cross-shelf survey on 27 January 2009 (details in Brown et al., 2009). The hydrographic water property section revealed a relatively well-mixed water column (< 0.26 sigma-t units) in that part of the study region shoreward of the 50 m isobaths. The weak salinity-induced density stratification was very similar to that reported upon by Shcherbina and Gawarkiewicz (2008), who measured hydrography a few kilometers north of our study site during a recent winter.

High frequency radar surface current measurements: The tidal eddy motion of interest was discovered in surface current maps derived from a pair of long-range 5 MHz HF radars facing eastward from Nauset and Nantucket, MA respectively (see Fig. 2). The 100-watt Coastal Ocean Dynamics Application Radar (CODAR) instrumentation used transmits a continuous sequence of 40 μs sweep frequency radar pulse/blank pair eastward from Cape Cod (and Nantucket) through an approximate 150-degree azimuth. Portions of those radar transmissions are backscattered to the CODAR site receiver from surface ocean waves in the “field of view” at ranges between about 5 km beyond the beach and a maximum of about 200 km offshore (depending upon transmission conditions). Using Doppler theory, each site measures the radial components of the ocean surface velocity directed toward or away from the site (Crombie, 1955; Barrick, 1972; Barrick et al., 1977). Since the systems are using surface gravity waves to estimate these velocity components, the measured currents at this frequency are the weighted average of the currents within the upper 1 m of the water column (Stewart and Joy, 1974). The radial data in the region of overlap were combined into hourly averaged total surface current vector maps on a fixed grid using the CODAR Ocean Sensors software package. Kohut and Glenn (2003) have shown that the noise in the returned radar signal can be reduced sufficiently with an hour of averaging to produce meaningful radial surface current estimates. The quality of the CODAR radial current measurements has been assessed by several investigators. For example, Kohut and Glenn (2003) find that the nominal spatial resolution of the surface currents is about 6 km and an accuracy of about 5 cm/s when the

Table 2

Basic statistics of the bottom pressure and 2 m bin-averaged ADCP currents at depths of 8 m and 6 m above the bottom (AB) at station TTE; with an average depth of 13 m. The current ellipses are given in terms of major axis amplitude, direction and ellipticity (ϵ =major/minor).

Station TTE	Mean (cm/s)	SD (cm/s)	Var (cm/s) ²	Total Var (cm/s) ²	Major Axis Amp (cm/s)	Major Axis Dir (°T)	ϵ
Currents							
8 m AB							
Northward	-8.5	30.9	954				
Total	-4.1	17.2	295	1249	35.1	19	8.1
Eastward							
6 m AB							
Northward	-8.0	29.3	859				
Total	-4.1	16.1	259	1118	33.2	19	8.9
Eastward							
Average							
Northward	-8.2	30.1	904				
Total				1180	34.1	19	7.8
Eastward							
Pressure							
1 m AB			(dbar)				
Total			0.851				
				(dbar ²)			
				0.724			

CODAR antenna beam patterns for the respective sites have been measured.

Moored measurements: A bottom-mounted instrument package, with an upward-looking RD 300 kHz Workhorse Acoustic Doppler Current Profiler (ADCP) and Aanderaa TR-7 pressure sensor (see Brown et al., 2009), was deployed off of Chatham, MA at station TTE ($41^{\circ} 39.5'N$ $69^{\circ} 55.4'W$) on 3 November 2008 and recovered on 27 January 2009 (see Table 1). We recovered a 2.5-month record of 5-minute bottom pressure (BP) samples (Table 2), with an estimated statistical uncertainty of ± 0.10 dbar. We recovered approximate 2 month records of 10-minute average ADCP currents, with an estimated uncertainty of ± 0.05 m/s, at 6 m and 8 m above the bottom. The moored current measurements compared very favorably with a set of overlapping 4 November 2008, higher resolution shipboard 1200 kHz ADCP current measurements as described by Marques and Brown (2009).

3. Numerical modeling

The Lynch et al. (1996, 1997) high-resolution finite-element coastal ocean circulation model QUODDY was employed to simulate the tide-dominated currents in the study region. The weak stratification during the study period justified our use of the barotropic mode of QUODDY. The model was forced with hindcast 5-constituent (M_2 , N_2 , S_2 , O_1 , and K_1) sea level along the open ocean boundaries of the model domain; as defined by the Holboke (1998) unstructured mesh called GHSD (see Fig. 3). The model lateral resolution in this application varied from about 10 km in the Gulf of Maine (GoM) interior, to about 5 km near the coastlines, with even finer kilometer-scale resolution in the regions of steep bathymetric slopes (e.g., north flank of Georges Bank). The vertical structure was resolved with 21-sigma layers from the 10 m minimum depth at the coastal boundary elements throughout the model domain. The model results considered here were produced every 1/16th M_2 tidal cycle for the time periods of simulation.

QUODDY is a 3-D, nonlinear, prognostic, f-plane, finite-element coastal ocean circulation model with advanced turbulence closure (Lynch et al., 1996; 1997). In this application, bottom flow \vec{V}_b is subject to quadratic bottom boundary stress, according to $C_d|V_b|V_b$, where the initial time/space constant bottom drag coefficient C_d was 0.005; followed by a simulation with a time/space constant $C_d=0.010$. There was no surface forcing imposed for this study.

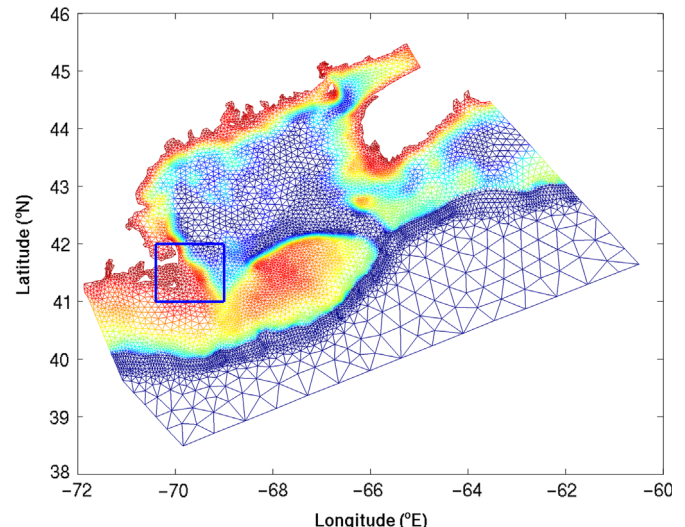


Fig. 3. The greater Gulf of Maine region is partitioned with the Holboke (1998) finite-element mesh (GHSD) that is used with the 3-D finite element coastal ocean model – QUODDY. The study region is defined. The color-coded depths (m) are defined in Fig. 4. (For interpretation of the references to color in this figure legend, the reader is referred to the web version of this article.)

The conditions imposed on the different QUODDY open ocean boundaries are for:

- **Deep ocean and the northeastern and southwestern cross-shelf sections:** Hindcast semidiurnal M_2 , N_2 , S_2 and diurnal K_1 and O_1 elevation series, based the Mukai et al. (2002) EastCoast 2001 tidal harmonics database that was derived from a harmonic analysis of simulations of ADvanced CIRCulation (ADCIRC) finite-element hydrodynamic numerical model.
- **Bay of Fundy section:** Hindcast Normal flows for the M_2 , M_4 , M_6 , N_2 , S_2 , K_1 and O_1 tidal constituents based on the harmonic constants derived from a simulation using the linear numerical model FUNDY6 – a predecessor of QUODDY with linear dynamics.

The barotropic QUODDY model calculation, which was initialized with zero velocity and elevation fields, was run with a

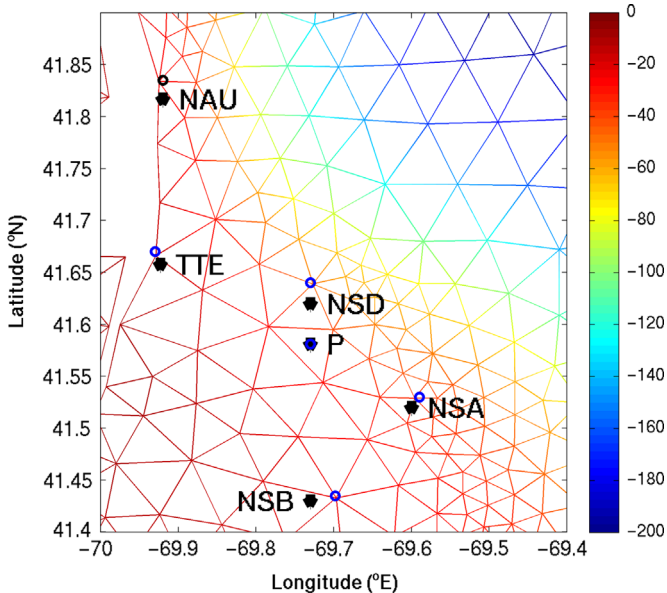


Fig. 4. This is a zoom showing the model resolution in the region of the observation (triangles) and model (circles) stations. Time series from these corresponding stations are compared. The color bar defines the depths in meters. (For interpretation of the references to color in this figure legend, the reader is referred to the web version of this article.)

21.83 s (=the 12.42-hour M_2 tidal period/2048) time-step. To allow the model to reach dynamical equilibrium, the amplitude of the prescribed tidal forcing was linearly increased to full forcing (i.e., ramped-up) during the first six M_2 tidal cycles of the model run. Holboke (1998) has shown that the QUODDY advection and nonlinearities dynamically adjust to the initial fields with such a ramp-up.

Marques and Brown (2009) found that the quality of this QUODDY model application (with 5-tidal constituent forcing) was generally very good in terms of model minus observation differences of the harmonic constants at the Moody et al. (1984) 49-stations. The differences were particularly small for the M_2 tidal sea level amplitudes, with a percentage mean, mean \pm standard deviation of differences between the observation-based and the mean and standard deviation of the M_2 tidal sea level amplitudes were 7.7%, 0.051 ± 0.045 m; phases were $3.5 \pm 3.8^\circ$ G, respectively. The corresponding percentage mean difference, mean \pm standard deviation for N_2 were 13.6%, 0.026 ± 0.022 m; phases were $12.2 \pm 6.0^\circ$ G; for S_2 were 18.0%, 0.030 ± 0.019 m; phases were $15.1 \pm 9.7^\circ$ G; for K_1 were 28.0%, 0.022 ± 0.017 m; phases were $11.2 \pm 8.2^\circ$ G; and for O_1 were 10.8%, 0.009 ± 0.008 m; phases were $8.9 \pm 9.5^\circ$ G, respectively.

4. Results

4.1. Observational results

The sequential pair of hourly CODAR surface current maps (Fig. 5) from 27 January 2009 are consistent with the development of CW eddy motion, upon which we focus. The robustness of the tidal motions underlying these CODAR maps is demonstrated in the moored current results.

The moored ADCP provided time series of 2 m bin-averaged currents at 6 m and 8 m above bottom (AB). The statistical similarity between these current fluctuations (see Table 2) prompted us to produce the vertically averaged TTE ADCP current records that are presented in Fig. 6. The series mean flow of 0.092 m/s towards 206° T

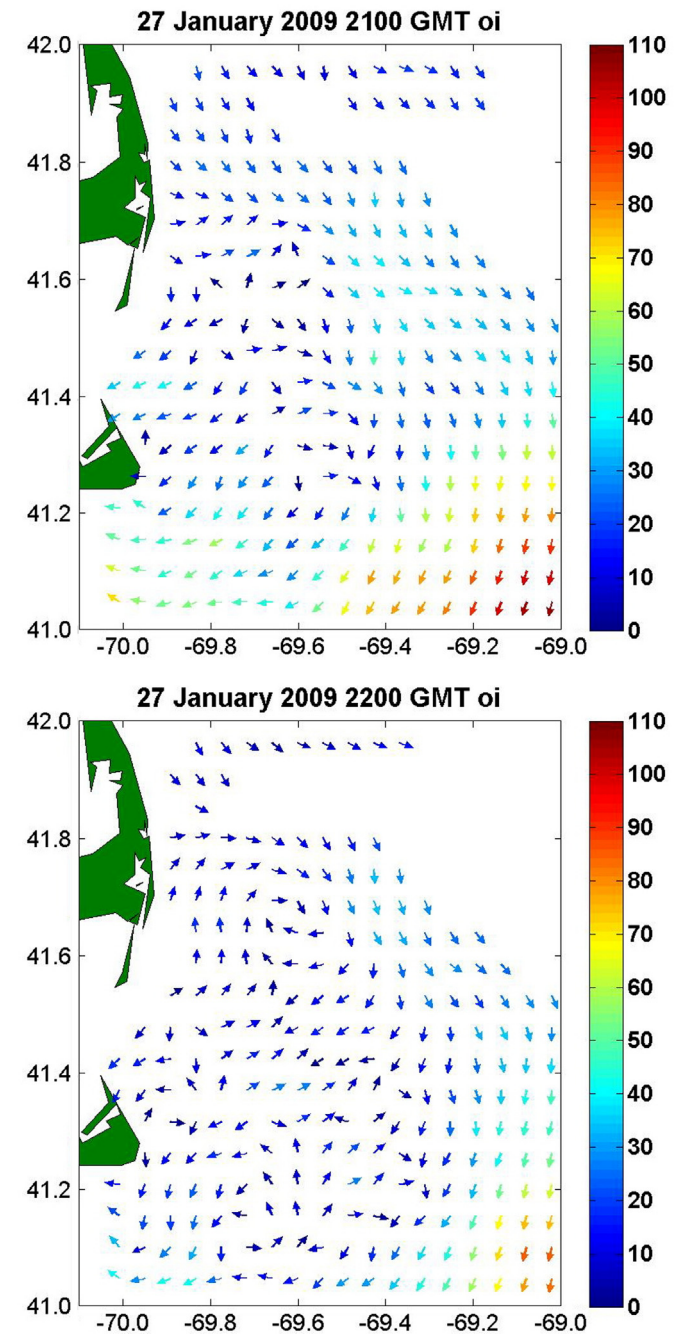


Fig. 5. Region-scale CODAR-derived surface current fields for 27 January 2009 (above) 2100 GMT and (below) 2200 GMT.

(detailed in Table 2) is nearly aligned with the much stronger fluctuating flow with a highly polarized variability ellipse with a 0.341 m/s major axis and orientation along $19\text{--}199^\circ$ T. About 50% of the mean current can be attributed rectified tidal current flow as determined by our model results (see below).

The results of a harmonic analysis of the moored current time series at station TTE show that the fluctuating currents are dominated by nearly identical M_2 tidal currents, with near-rectilinear motions oriented along $30\text{--}210^\circ$ T (see Fig. 7; Table 3; Appendix A). (The energy of the non-tidal residual series was about 1/10 of that of the full series – emphasizing the dominance of the tidal response of the region.) High-resolution USGS bathymetry shows that the station TTE tidal currents are aligned with grooves seen in the local bathymetry. The spring-neap cycles that

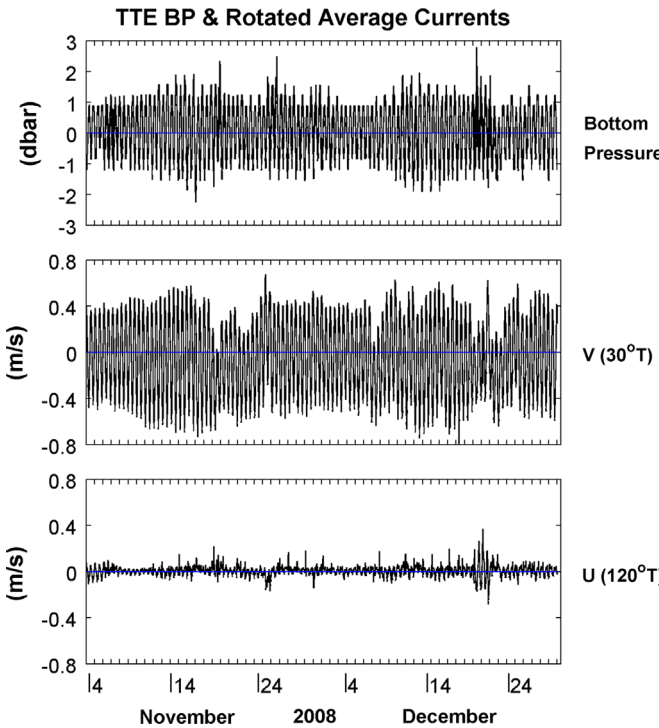


Fig. 6. Station TTE (upper) bottom pressure; and vertically averaged (middle) 30°T-ward and (bottom) 120°T-ward currents.

are associated with these measurements are highlighted in Fig. 7, which features a set of 85-day tidal hindcast records for the November 2008 – January 2009 study period.

The dominance of the semidiurnal tides in the bottom pressure and currents at station TTE convinced us to augment the TTE records with a tidal hindcast records of (a) bottom pressure (BP) at a station just offshore of Nauset, MA (NAU) and (b) currents at stations NSA, NSD, and NSB, respectively (see Table 1; Fig. 2). These tidal hindcast series were generated using the available tidal harmonic constants (Moody et al., 1984) for the five principal tidal constituents, namely the three most important semidiurnal constituents (M_2 , N_2 , and S_2) and the two most important diurnal constituents (O_1 , and K_1). We focus our attention on the depth-averaged currents at TTE and NSA and the single mid-depth currents at stations NSD and NSB. (Note: Comparisons with the depth-averaged current at NSA indicate that the mid-depth currents NSD and NSB are reasonable approximations of the local depth-averaged currents.)

As shown in Fig. 7, the major axes of the dominant M_2 tidal current ellipses at the current stations in our study region are generally oriented in the northeastward-southwestward direction (see details in Table 4). Further we note that there are statistically significant phase differences between the different maximum M_2 tidal current inflows. Below we show how these phase differences are induced by the alternating tidal eddy motions. (See Appendix A for more complete harmonic constant lists.)

The general northeast–southwest orientation of the dominant M_2 tidal current ellipses prompted us to rotate our analysis coordinate system 30° clockwise (see Fig. 7) so that it was more naturally aligned with the dominate tidal currents. In the rotated coordinate system Y and V point toward 30°T; and X and U toward 120°T. However, station NSB was significantly outside our defined study region. Thus we interpolated between the highly coherent tidal currents at stations NSB and NSD to produce tidal currents at a virtual station P inside the study region (see Fig. 8). Given the significant average depth difference (~30%) between the western (23 m) and eastern (33 m) parts of our rotated study

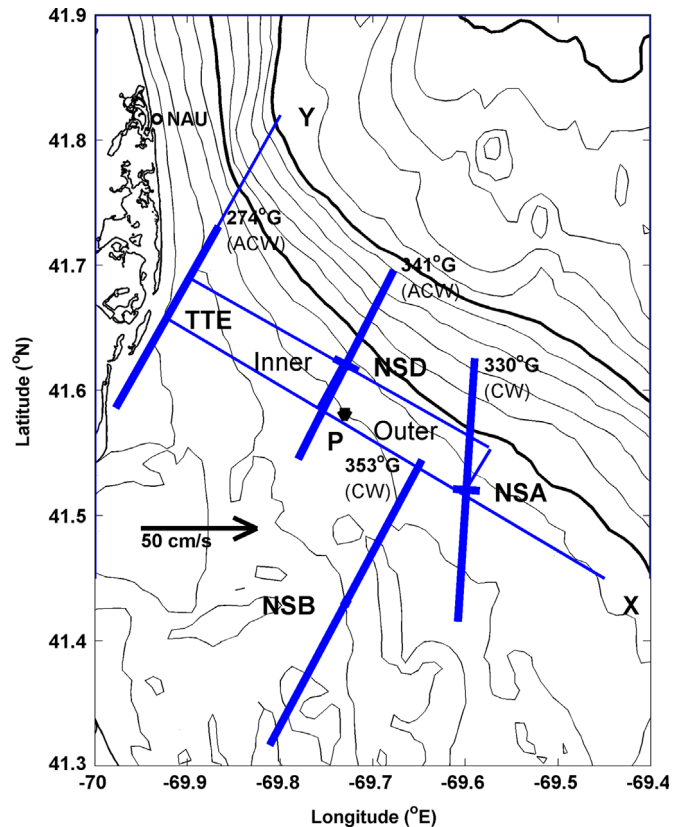


Fig. 7. A location map of the current and bottom pressure (o) stations in the rotated coordinate system (+Y towards 30°T). The tidal currents at station P were derived from a weighted-average of tidal hindcast tidal currents at NSA and NSD (see text). A shallower (average depth=23 m) *Inner Zone* and a deeper (average depth=33 m) *Outer Zones* are defined. The study region isobaths are given in 10 m intervals from the coast to 100 m; then 20 m intervals into deeper waters; with bolder 50 m, 100 m, and 200 m isobaths. The M_2 tidal ellipse major/minor axes (thick lines with scale lower left) at the observation stations TTE, NSD, NSA, and NSB. The Greenwich epoch phases (convention: lower values lead higher) of the maximum flood current at each of the stations and sense of current vector rotation (...) are also given.

region, we defined the shallower *Inner Zone* and a deeper *Outer Zone* shown in Fig. 7. The M_2 harmonic constants for these *rotated currents* at station P and the other current stations are given in Table 4. The 5-constituent hindcast of the rotated currents at stations TTE, NSD, NSA and P constitute the *observed current data set* used in the following analyses.

The M_2 tidal current displacement ellipses in the study region have very similar 50 km amplitude water parcel excursions along 30–210°T (see Fig. 6), but different phases. In particular, the TTE maximum M_2 current leads other current max phases by 55–70° (~2.4 h). As we will show later, these phase differences are the signatures of the alternating anticlockwise (ACW) and clockwise (CW) eddy motions that traverse the study region.

It is also noteworthy that the M_2 tidal current vectors in the IZ rotate ACW, while those in the Outer Zone rotate CW (Table 4). Thus our study region appears to be located in the transition zone between progressive Sverdrup M_2 tidal wave and near-standing wave regimes; where Brown (1984) has defined in association with Georges Bank and the GoM proper, respectively.

4.2. Model results

The regional kinematics of the tidal eddy motion formation and evolution are revealed in the sequence of model ($C_d=0.005$) surface current maps in Fig. 9a–g. The first in the sequence at

Table 3

The harmonic constants for the 5 principal + 2 nonlinear tidal constituents of the station TTE depth-averaged eastward and northward current components (based on 56-day records starting 3 November 2008); given in terms of sinusoidal amplitudes and Greenwich epoch phases. The current vector ellipses are given in terms of major axis amplitude/orientation and ellipticity (ε =major/minor; where positive values mean anticlockwise-rotating current vector), and maximum current Greenwich epoch phase.

Tidal Const.	East Amp (cm/s)	Phase (°G)	North Amp (cm/s)	Phase (°G)	Major Axis Amp (cm/s)	Major Dir (°T)	ε	Phase (°G)
M₂	22.2 ± 0.5	272 ± 1	39.7 ± 1.1	275 ± 1	45.5	29	38	274
N₂	3.8 ± 0.5	244 ± 7	6.8 ± 1.1	252 ± 8	7.8	29	16	250
S₂	2.1 ± 0.5	312 ± 12	6.5 ± 1.1	313 ± 9	6.9	18	∞	313
K₁	0.9 ± 0.5	299 ± 30	1.6 ± 1.1	260 ± 37	1.8	26	-4	176
O₁	0.3 ± 0.4	328 ± 75	0.1 ± 0.1	216 ± 106	0.3	274	-3	237
M₄	1.1	143	2.3	173	2.3	23	4	256
M₆	0.9	17	0.7	33	1.1	52	11	226

Table 4

The M₂ constituent harmonic constants for the observed rotated station (a) depth-averaged currents at TTE and NSA; (b) mid-depth currents at NSB (10 m) and NSD (16 m); (c) interpolated currents at P; (d) Inner Zone (IZ) currents=TTE-P average; and (d) Outer Zone (OZ) currents from NSD and NSA. The harmonic amplitudes and Greenwich epoch phases are given along with the M₂ tidal current ellipse in terms of major axis amplitude and orientation, ellipticity (ε =major/minor for which a positive value indicates an anticlockwise rotating current vector), and the phase of the maximum current. Notice the consistency in the clockwise and anticlockwise rotation of the IZ and OZ average current vectors with the individual station ellipse characteristics, respectively.

Stations	Sta Dep (m)	U Amp (cm/s)	U Ph (°G)	V Amp (cm/s)	V Ph (°G)	Major Amp (cm/s)	Major Dir (°T)	ε	Max Ph (°G)
TTE	13	1.3	181	47.1	275	47.1	30	36	275
P	30	3.6	165	51.4	345	51.5	26	517	345
NSD	33	6.4	226	45.9	341	46.0	27	8	341
NSA	33	26.0	139	51.5	333	57.4	4	-10	330
NSB	23	19	91	71	354	71	28	-4	353
Inner Zone	23	3	162	40	312	40	27	33	312
Outer Zone	32	14	153	49	337	51	14	-51	337

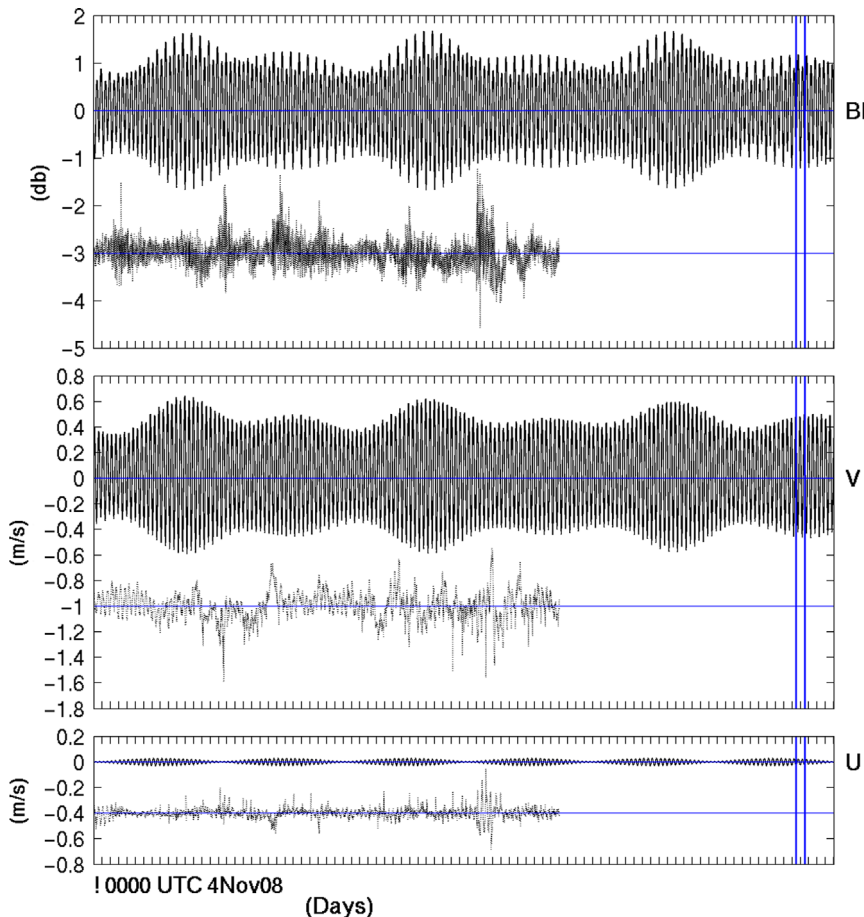


Fig. 8. The station TTE hindcast tidal (solid) records for (upper) bottom pressure (BP), (middle) vertically averaged 30°T-ward (V) and (lower) 120°T-ward (U) currents for the 4 November 2008 through 31 January 2009 study period. The residual series from which the hindcast tide has been removed (dotted) are offset for clarity. The principal 27–28 January 2009 analysis period is bracketed by the pair of vertical lines to the right.

1759⁵¹ GMT 27 January 2009 (Fig. 9a) shows a robust ebb flow spanning the Great South Channel (GSC). We define this flow configuration as EBB_{full} – the reference time for the half tidal cycle explored with following. The superscripts on the time references refer to seconds.

Between EBB_{full} and EBB_{full}+2.55 h (2032 UTC Fig. 9b), the near-coast, laterally sheared Coastal Boundary Layer (CBL) gradually bulges offshore displacing the core of the main along-shore tidal flow. As we will show below, this CBL bulge buffers the interior ebb flow which is slowing, stalling leading

to the formation of a small-scale nearshore clockwise (CW) eddy motion.

By 2043 UTC (EBB_{full}+2.72 h; Fig. 9c), the model surface current maps show distinct CW eddy motion near the coast. This marks the onset of the northward flood tidal flow in the western GSC during this phase in the semidiurnal tidal cycle.

By 2053⁰² UTC (EBB_{full}+2.88 h; Fig. 9d), the CBL separates from the coast as the CW eddy motion center (EMC) begins to translate seaward. This translating eddy motion is signaling the onset of flood flow in the western GSC.

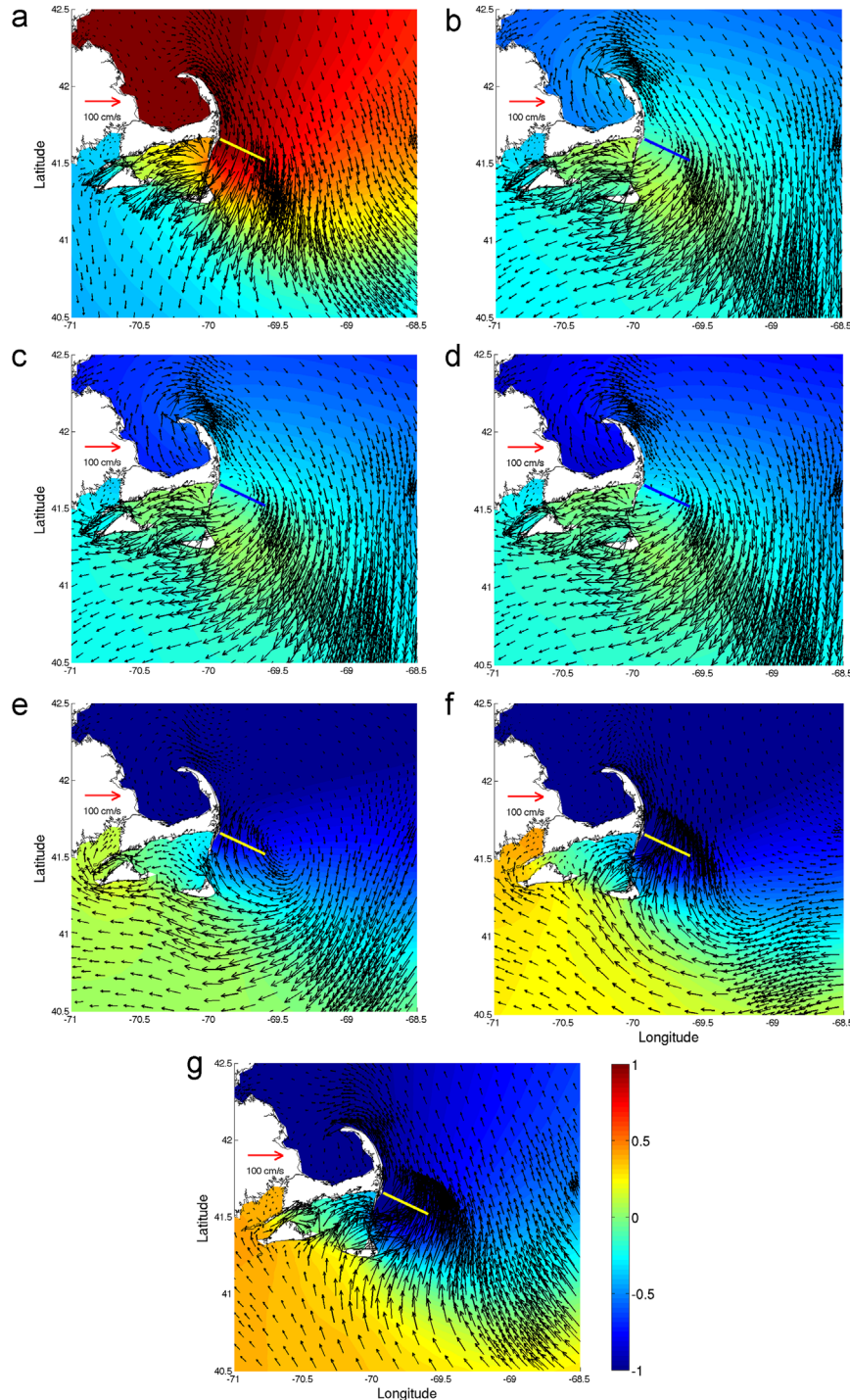


Fig. 9. Model surface current and color-coded sea level (m) for 27 January 2009 at: (a) EBB_{full} + 0.00 h (1759⁵¹ UTC); (b) EBB_{full} + 2.55 h (2032⁴⁰ UTC); (c) EBB_{full} + 2.72 h (2042⁵¹ UTC); (d) EBB_{full} + 2.88 h (2053⁰² UTC); (e) EBB_{full} + 4.07 h (2204²¹ UTC); (f) EBB_{full} + 5.09 h (2305²⁸ UTC); (g) EBB_{full} + 6.28 h (0016⁴⁷ UTC); The yellow or blue bars span stations TTE and NSA. (For interpretation of the references to color in this figure legend, the reader is referred to the web version of this article.)

By 2204 UTC (EBB_{full} + 4 h; Fig. 9e), the expanding/weakening CW EMC has translated about 44 km offshore toward the south-east of Chatham; accompanying the rapidly translating onset of flood flow.

Between 2204 and 2305 UTC (EBB_{full} + 5 h; Fig. 9f), the CW EMC “raced” eastward across most of the GSC.

By 0016⁴⁷ UTC 28 January (EBB_{full} + 6.28 h; Fig. 9g), the complete changeover from ebb to flood tidal flow across the whole GSC has occurred. With the establishment of a robust flood flow across the GSC (or FLOOD_{full}) marks the beginning of the process during which the ACW eddy motion forms near the Cape Cod coast.

As shown by the model surface current map at 0158 UTC (EBB_{full} + 7.98 h; map not presented here), the strengthening

northward flood flow separates from the coast (much like the southward ebb flow 6 h earlier). Within the following hour, ACW motion (counterpart of the CW eddy motion) develops near the coast. Over the next 3 h, the evolution and translation of the ACW eddy motion mirrors that of the CW eddy motion evolution in issuing the signal of upcoming ebb flow across the full GSC; thus completing the semidiurnal tidal cycle.

From an inspection of the full suite of Fig. 9a–g model surface current maps (temporal resolution = 1/16 M₂ tidal cycle), we constructed a fine scale track of the eddy motion center across our near-coastal study region. The seaward migration of the model CW EMC across the study region between 2043 and 2204 UTC is mapped in Fig. 10. In the next section we assess the fidelity of the model picture of the eddy motion generation and evolution by comparing model and observation results.

The observed time series are compared with model time series at mesh nodes that were within 4 km of the respective observation stations (see Table 5). The comparisons between observed and model results were best done with their respective 5-tidal constituent hindcast time series because all of the observed series, except at station TTE, were limited 5-tidal constituent hindcast series. This meant however that, except at station TTE, we could not explore differences related to hydrodynamics-related non-linear harmonic constituents, such as M₄, M₆, S₄, and S₆; which usually contribute to the distortion of the sinusoidal ocean tidal responses of the model and measured Gulf of Maine (GoM).

4.3. Observation–model comparisons

A comparison between observed and a preliminary set of model depth-averaged M₂ tidal current ellipses revealed that the model current amplitudes were significantly greater than the observed currents (see Table 5). For example, the model station NSA M₂ current variances were about 80% greater than their observed counterparts. This observation/model difference, which was documented for currents across the array, prompted us to increase the model bottom friction from an initial space/time constant bottom drag coefficient from C_d=0.005 to C_d=0.010 in a subsequent model run. The model currents in the C_d=0.010 run (henceforth referred to as model₀₁) were significantly less energetic than those from the model₀₀₅ run (see Table 5). Although we could have chosen to tune the model bottom friction to provide “better” currents in the model, that was not the purpose of the study. So in subsequent analyses below, we used the model₀₁ results.

Fig. 10. Clockwise eddy motion center (EMC) locations (bold circles) were derived from model surface current maps of the eddy motion as it translated across the study region – between 2032 and 2204 UTC 27 January 2009. The isobaths are given in 10 m intervals from 10 m to 100 m and then 20 m intervals seaward of the 100 m isobath.

Table 5

The M₂ constituent harmonic constants for the observed (obs) rotated, depth-averaged current components (U – 120°T; V – 30°T) at sites TTE, NSD and NSA are given in terms of amplitudes, Greenwich epoch phases, and total variances. The associated current ellipses are given in terms of major axis amplitude and orientation, ellipticity (ε = major/minor, with a positive values indicating an anticlockwise rotating current vectors), and the Greenwich phase of the maximum current. Harmonic constants are also given for The model currents: w/C_d=0.005 > mod_{0.005}; w/C_d=0.010 > mod_{0.01} respectively at corresponding sites; based on 30-day simulation records.

Station	Dep (m)	Lat (°N)	Lon (°W)	Total Var (cm/s) ²	U Amp (cm/s)	U Ph (°G)	V Amp (cm/s)	V Ph (°G)	Maj Amp (cm/s)	Dir (°T)	ε	V _{max} Ph (°G)
NSA – obs	33	41.52	69.60	1664	26.1	139	51.8	333	57.7	4	-10	330
– mod _{0.01}	40	41.53	69.59	1874	27.3	149	54.8	344	60.9	4	-9	341
– mod _{0.005}	40	41.53	69.59	2874	32.9	143	68.3	342	75.1	5	-8	339
NSD – obs	33	41.62	69.73	1074	6.4	226	46.1	341	46.1	27	8	341
– mod _{0.01}	50	41.64	69.73	998	18.2	153	40.8	323	44.6	6	15	325
– mod _{0.005}	50	41.64	69.73	1553	21.8	150	51.3	319	55.6	7	15	321
TTE – obs	13	41.66	69.92	1036	1.3	155	45.5	274	45.5	29	38	274
– mod _{0.01}	10	41.67	69.93	1423	10.5	92	52.3	307	53.0	21	-9	306
– mod _{0.005}	10	41.67	69.93	2355	12.4	91	67.5	303	68.3	21	-11	302
P – obs	30	41.58	69.73	1338	3.6	164	51.6	345	51.7	26	-517	345
– mod _{0.01}	30	41.58	69.73	1358	18.0	136	48.9	331	51.9	10	-12	329
– mod _{0.005}	30	41.58	69.73	1628	19.3	139	53.7	329	57.0	11	-17	328

Differences between the *observed* and *model₀₁* 5-constituent hindcast time series at various stations are illustrated for the 25-hour segments spanning 27–28 January 2009. For example, the amplitudes and phases of the *observed* and *model₀₁* V velocity components at stations NSA and NSD (V_{NSA} – Fig. 11b; V_{NSD} – Fig. 11c) are within $\pm 10\%$. To quantify the observation–model differences, we define a variance ratio (VR);

$\text{VR} = (O - M)_{\text{var}} / (\text{Ave } OM)_{\text{var}}$, where $(O - M)_{\text{var}}$ is the *observed* minus *model₀₁* records and $(\text{Ave } OM)_{\text{var}}$ is the variance of the average of the *observed* and *model₀₁* records. By this measure, the V_{NSA} and

V_{NSD} comparisons were relatively good with $\text{VR}_{\text{NSA}} = 0.043$ and $\text{VR}_{\text{NSD}} = 0.159$, respectively. The *observed* versus the *model₀₁* V_{TTE} comparison (Fig. 11d) was not as good ($\text{VR}_{\text{TTE}} = 0.426$); due mainly to the relatively larger *observed* versus *model₀₁* phase difference.

Current difference comparisons: The X-lateral V current difference [e.g., for the IZ del_x $V^{\text{IZ}} = (V_{\text{NSD}} - V_{\text{TTE}})$] is a potentially important diagnostic of eddy motion because it (1) contributes significantly to regional vorticity estimates (i.e., $\delta v / \delta x - \delta u / \delta y$); and (2) can be measured in real time (via CODAR and/or via telemetry from moorings). Thus we seek to understand its use in

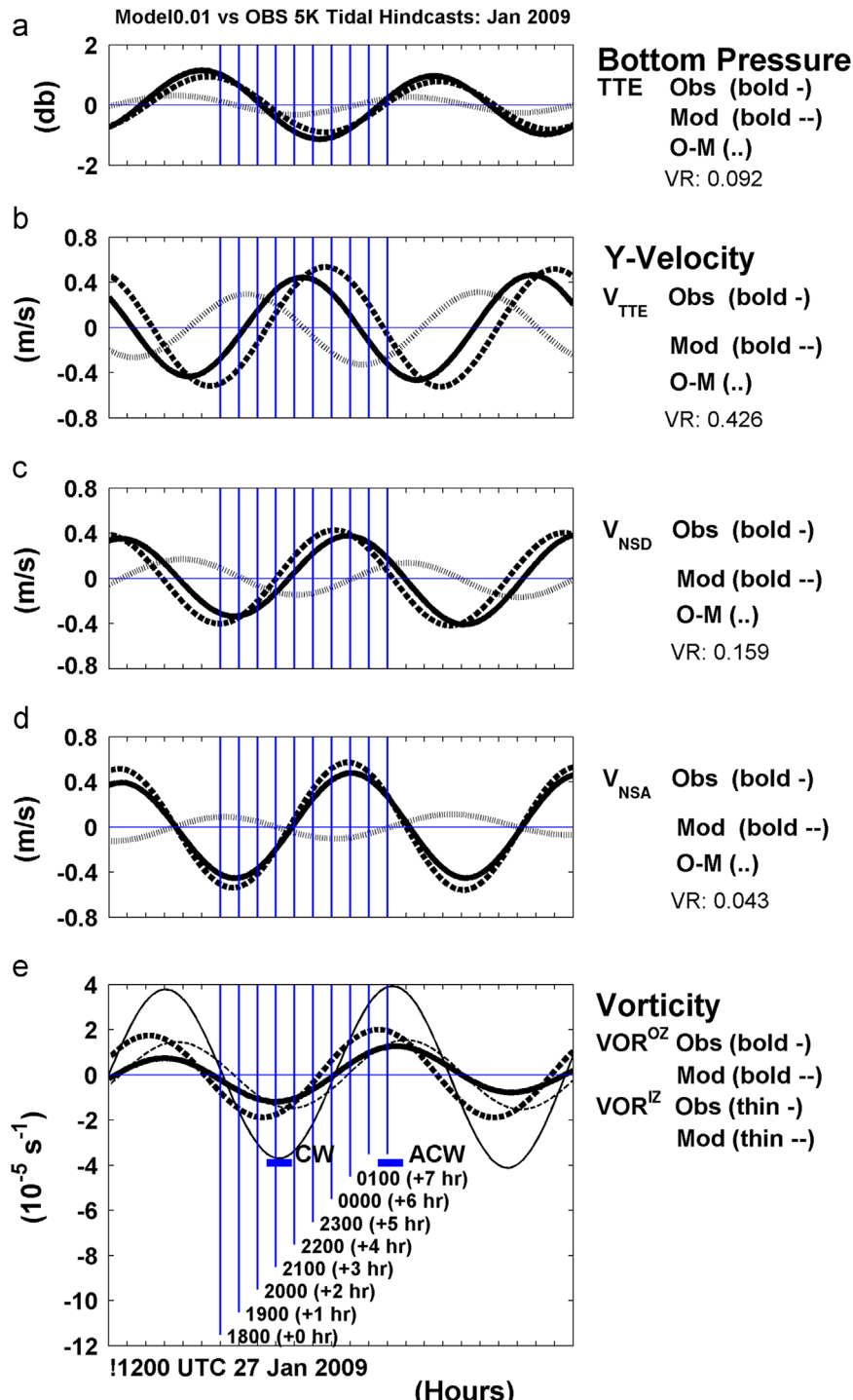


Fig. 11. Comparisons of *observed* (OBS) and *model₀₁* (MOD) 5-constituent tidal hindcast series in terms of observed minus *model₀₁* ($O - M$) difference series for: (a) TTE bottom pressure; (b) V_{TTE} ; (c) V_{NSD} ; (d) V_{NSA} ; and (e) vorticity for the Inner Zone (VOR^{IZ}) and Outer Zone (VOR^{OZ}) respectively. A measure of the quality of the comparisons is the variance ratio $\text{VR} = (O - M)_{\text{var}} / (\text{Ave } OM)_{\text{var}}$ (see main text).

diagnosing eddy motion. This task is challenging because differencing currents usually exaggerates uncertainties in the measurements. So what is the situation in our study region? On one hand, the OZ $model_{01}$ [$\text{del}_x V^{OZ} = (V_{NSD} - V_{TTE})$; not shown] is about two times greater than and lags the observed $\text{del}_x V^{OZ}$ by about 3/4 h. On the other hand, observed and $model_{01}$ Y-lateral U current differences [$\text{del}_y U^{OZ} = (U_{NSD} - U_p)$ – not shown] are almost identical in amplitude and phase, and much smaller in amplitude. There is also a significant difference between the observed and $model_{01}$ $\text{del}_x V^{IZ}$ [= $(1/2)(V_{NSD} - V_{TTE})$] records. This difference is mainly due to an observed V_{TTE} (a 13 m water column) which is much weaker (relative to observed V_{NSD}) than is the $model_{01}$ V_{TTE} . This could be due to an observed bottom friction which is larger than its modeled counterpart.

Vorticity comparisons: Here we define Outer Zone vertical vorticity as

$\text{VOR}^{OZ} = (\text{del}_x V^{OZ}/\delta X - \text{del}_y U^{OZ}/\delta Y)$, where δX and δY are the respective spatial separation distances. Interestingly, we find that the observed and $model_{01}$ OZ vorticity time series (Fig. 11d) are in phase; despite a factor of two amplitude difference. The significantly larger observed $\text{del}_x V^{IZ}$ noted above contributes to an observed VOR^{IZ} which is significantly larger than the $model_{01}$ VOR^{IZ} .

Bottom pressure comparisons: The comparison between the station TTE $model_{01}$ and observed BP harmonic constants (see Appendix A – Table A1) shows that the $model_{01}$ M₂ BP amplitudes were about 20% less than those observed; but were within 8° in phase. The observed and $model_{01}$ 5-constituent hindcast BP record amplitudes at station TTE are consistent with that result (see Fig. 11a). Based on a comparison between TTE study region observation- and model-based estimates of the horizontal pressure gradients (PG) from measurements (e.g., Nauset minus TTE BP), Brown and Marques (2012) concluded that their spatial scales of these PG estimates were too large to be useful in the smaller scale dynamics considered below. Because the $model_{01}$ sea levels and sea level gradients were available on the 1–3 km scales of the model mesh finite element spacing (see Fig. 4), we used BP and BP gradient which were hydrostatically derived from the $model_{01}$ sea levels and sea level gradients.

We conclude from these model-observation current comparisons that the real bottom stresses in our study region are larger than “normally” parameterized (i.e., $C_d = 0.005$) model bottom stresses. Perhaps the “bumpiness” in the bottom bathymetry generates a form drag that augments the frictional bottom stresses. In any case, using $C_d = 0.01$ produces momentum balances (i.e., dynamics) that

are in significantly better agreement with observations than when $C_d = 0.005$ is used in the model.

Despite the differences discussed above, the observations and the $model_{01}$ are presenting very similar pictures. These observation–model time series comparisons indicate enough consistency that we are encouraged to explore the usefulness of the observed current differences and zonal average vorticity time series as proxies of the eddy motion formation and evolution process in our study region. That analysis follows.

5. Eddy motion formation process

Here we breakdown the continuous tidally driven process which spawns a non-ending sequence of alternating eddy motions that are highlighted in Table 6. We break into the continuous process at EBB_{full} – just after maximum ebb flow in the Inner Zone (i.e., IZ V; see Fig. 12c) at 1800 UTC on 27 January 2009.

At 1800 UTC:

- (a) Nearshore ebb flow begins to slow (i.e., V_{TTE} accelerates); This is because the station TTE Y-pressure gradient force ($model_{01}$ $\delta p_b/\delta Y$; Fig. 12b) is going positive in opposition to the local the ebb flow;
- (b) IZ lateral V current difference and vorticity go negative (see Fig. 12c and d); This is because V_{TTE} begins to exceed V_{NSD} ;
- (c) Negative-going $\text{del}_x V^{IZ}$, OZ–IZ $\text{del}_x V$, and VOR^{IZ} mark the beginning of CW eddy motion formation (before it is visually evident);

Between 1800 UTC and 2042 UTC (2.5 h):

There is a negative vorticity buildup within the CBL envelop (Fig. 9a–c); as diagnosed quantitatively by the sustained decrease in $\text{del}_x V^{IZ}$, OZ–IZ $\text{del}_x V$, and VOR^{IZ} (see Fig. 18d,e);

At 2052 UTC:

The CBL, with visible CW eddy motion (Fig. 9d) within its envelope, separates from the coast; as diagnosed by simultaneous minima in $\text{del}_x V^{IZ}$, OZ–IZ $\text{del}_x V$ (= $V_{NSD} - V_{TTE}$), and VOR^{IZ} (see Fig. 18d,e). Note in Fig. 10 that the center of the eddy motion (EMC) passes from the Inner to the Outer Zone at this time.

Table 6

Transient tidal eddy motion formation and evolution: 27–28 January 2009. The milestones are referenced to EBB_{full} or 1800 UTC – the time of maximum ebb flow throughout the Great South Channel (GSC) region. Reference is made to the status of the Coastal boundary Layer (CBL), the eddy motion center (EMC), and increases (↑) and decreases (↓) in intensity.

Time (UTC)	Fig. Ref.	Time rel EBB _{full} (hr)	Model tidal stage	Eddy motion formation and evolution process highlights
1557 ³⁶		–2.03	CBL ebb w/intensity ↑ GSC flood w/intensity ↓	ACW EMC/vorticity max translates seaward w/intensity ↓ and scale ↑
1659		–1.02	CBL ebb w/intensity ↑ GSC flow weak eastward	ACW EMC/vorticity max to center GSC w/intensity ↓
1759 ⁵¹	Fig. 9a	+0.00	EBB_{full} (ebb flow across full GSC)	Ebb _{max} – Inner Zone pgf _y ~0 reverses
1901		+1.02	CBL ebb w/intensity ↓ GSC ebb	Ebb _{max} – Outer Zone + pgf _y intensity ↑
2002 ⁰⁶		+2.03	CBL ebb w/intensity ↓ GSC ebb	+ pgf _y intensity ↑
2032 ⁴⁰	Fig. 9b	+2.55	CBL ebb stalls GSC ebb	+ pgf _y intensity ↑ ebb CBL separation
2042 ⁵¹	Fig. 9c	+2.72	CBL flow reverses GSC ebb	CW eddy motion forms near the coast
2053 ⁰²	Fig. 9d	+2.88	CBL flood w/intensity ↑ GSC ebb	CW EMC/vorticity min traverses Inner Zone
2103		+3.05	CBL flood w/intensity ↑ GSC ebb	CW EMC/vorticity min enters Outer Zone pgf _{y,max} in Inner Zone
2204 ²¹	Fig. 9e	+4.07	CBL flood w/intensity ↑ GSC ebb w/intensity ↓	CW EMC/vorticity min exits Outer Zone pgf _{y,max} in Outer Zone
2305 ²⁸	Fig. 9f	+5.08	CBL flood w/intensity ↓ GSC flow weak westward	CW EMC/vorticity min to central GSC + pgf _y intensity ↓
0016 ⁴⁷	Fig. 9g	+6.28	FLOOD_{full} (flood flow across full GSC)	Flood _{max} – Inner Zone + pgf _y ~0 reverses
0107		+7.12	CBL flood w/intensity ↓ GSC flood	Flood _{max} – Outer Zone – pgf _y intensity ↑
0159		+7.98	CBL flood stalls GSC flood	– pgf _y intensity ↑ flood CBL separation
0300		+9.00	CBL flow reverses GSC flood	ACW eddy motion forms near the coast

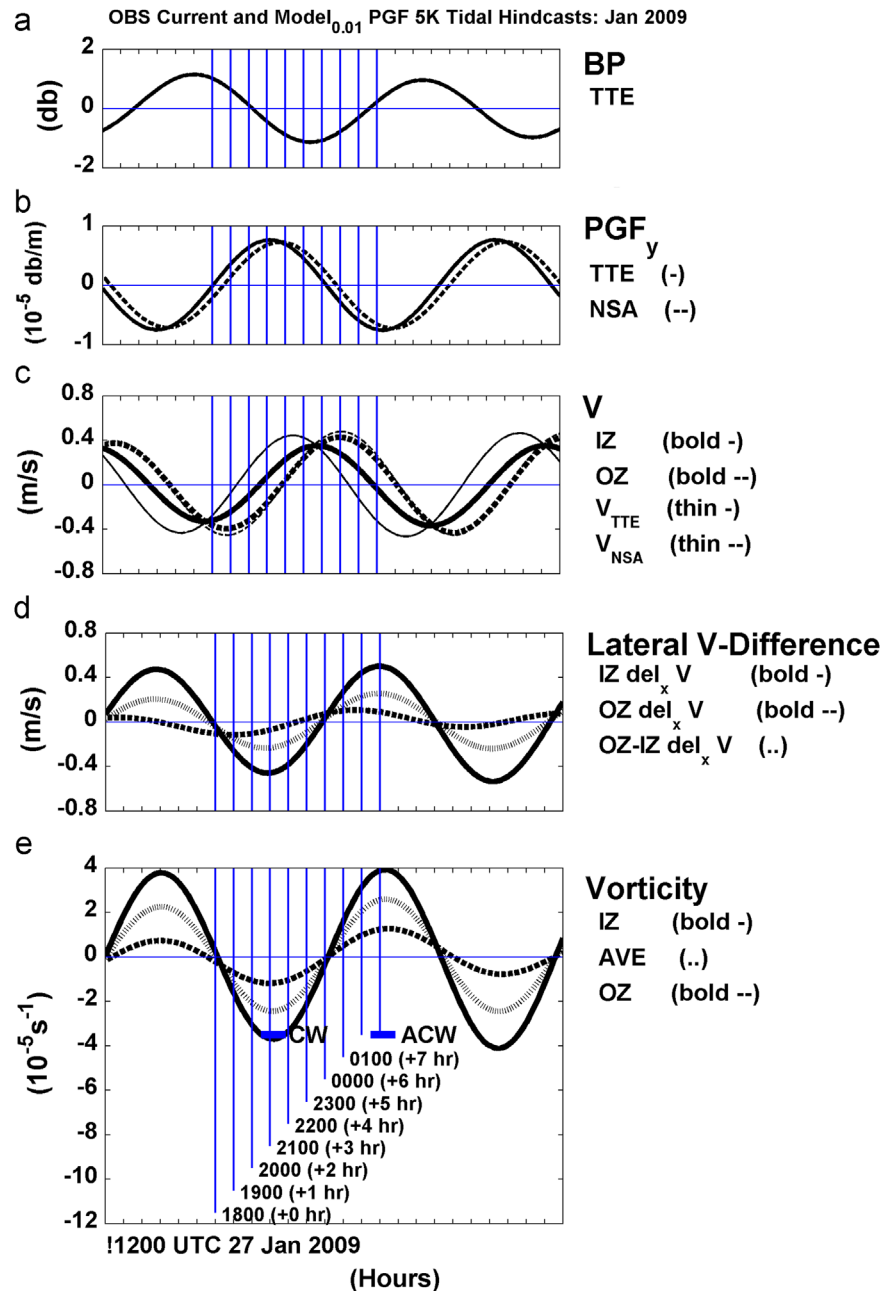


Fig. 12. Observed 5-constituent hindcast time series, including; (a) TTE bottom pressure; (b) model_{0.01} bottom pressure gradient forces ($-\delta p_b/\delta y$) at stations TTE and NSA; (c) observed IZ- and OZ-averaged V currents; (d) observed IZ-, OZ-, and OZ-IZ lateral current-difference $\delta_x V$ records (see text for definitions); and (e) observed IZ-, OZ-, and OZ-IZ- average vorticity. The vertical lines mark the hourly milestones in the flow kinematics (see Table 6), including durations of the CW and ACW eddy motion.

Between 2052 UTC and 2204 UTC:

The lateral scale of the negative vorticity CW eddy motion grows rapidly (see Fig. 9c,d). Consistent with that growth, the eddy motion center (EMC) migrates through the OZ at a rate of about 5 m/s (see Fig. 10). The CW eddy motion (with its relatively strong $-V$) passes by station NSA; as diagnosed by the transition of OZ-IZ $\text{del}_x V$ ($= V_{\text{NSA}} - V_{\text{TTE}}$) from increasing to decreasing.

Between 2204 UTC and 2305 UTC (Fig. 9e,f):

As the CW eddy motion (see the EMC ~ 2204 UTC in Fig. 10) migrates seaward, the seaward station V decreases relative to the landward station V ; as diagnosed by an increasing OZ-IZ $\text{del}_x V$ (Fig. 18d,e) – our proxy for the regional average vorticity. During the following 2 h (between EBB_{full}+3 h and EBB_{full}+5 h), the CW eddy motion's (a) EMC speed increases rapidly to ~ 25 m/s! as it

moves southeastward more or less along isobath across the GSC, (b) scale grows, and (c) strength weakens.

By 2416 UTC (0016 UTC 28 January; or EBB_{full}+6⁺ h): The CW eddy motion pattern disappears, as the ingoing tidal flow spans the entire GSC – at FLOOD_{full} (see Fig. 9g)

The ACW eddy motion results from a process which begins at FLOOD_{full}. Within about 2.5 h (at ~ 0230 UTC 28 January), the ACW eddy motion becomes well defined near the coast (not shown). It also grows in scale near coast over the next ~ 1.5 h and leaves the coast to cross the GSC with the full onset of ebb tidal flow – nearly mirroring the CW eddy motion formation and evolution.

Here we have shown that the $\text{del}_x V$ and VOR diagnostics track the kinematics of the flood to ebb ACW eddy motion formation

and evolution process just as well as they tracked the kinematics of the ebb to flood CW eddy motion counterpart. The dynamics of this process are explored next.

6. Eddy motion dynamics

In this section, we estimate the terms in the equations for conservation of the momentum and vorticity using both observations and model results. For momentum, we follow the Brown (1984) application of the volume-averaged momentum equations to a pair of arrays of measurements in the Gulf of Maine/Georges Bank region.

6.1. Momentum budgets

The following volume-averaged components of the momentum equations, in which surface horizontal stresses, minor lateral stresses, and stratification effects have been assumed to be negligible, are used (see Appendix B for the more detailed derivation). They are in *X-direction*:

$$\frac{\rho_o}{A} \left\{ \frac{\delta \langle U \rangle}{\delta t} + \langle \delta_x \bar{u} U \rangle_y + \langle \delta_y \bar{v} U \rangle_x - f \langle V \rangle + \frac{1}{\rho_o} \left\langle H \frac{\partial p_b}{\partial x} \right\rangle + \frac{1}{\rho_o} \langle \tau_x^b \rangle - \frac{1}{\rho_o} \langle \delta_y h T_x \rangle_x \right\} = 0 \quad (1a)$$

inertial A nonlinear B Coriolis pressure gradient horizontal stress lateral stress

Y-direction

$$\frac{\rho_o}{A} \left\{ \frac{\delta \langle V \rangle}{\delta t} + \langle \delta_x \bar{u} V \rangle_y + \langle \delta_y \bar{v} V \rangle_x + f \langle U \rangle + \frac{1}{\rho_o} \left\langle H \frac{\partial p_b}{\partial y} \right\rangle + \frac{1}{\rho_o} \langle \tau_y^b \rangle - \frac{1}{\rho_o} \langle \delta_x h T_y \rangle_y \right\} = 0 \quad (1b)$$

where U and V are the horizontal transport components, ρ_o is the reference water density (1025.7 kg m^{-3}), p_b is bottom pressure, τ^b is the bottom stress, and T is the vertically averaged lateral stress on the sidewalls of the study region, with an area $A = \Delta x \Delta y = (x_2 - x_1)(y_2 - y_1)$. The notation for the different integral and difference operators in Eq. (1) are

$$\begin{aligned} U/V &\equiv \int_{-h}^h u/v \, dz; \quad \dots \equiv \frac{1}{H} \int_{-h}^H \dots \, dz; \quad [\dots] \\ &\equiv \int_{y_1}^{y_2} \int_{x_1}^{x_2} \int_{-h}^h \dots \, dx \, dy \, dz; \quad \langle \dots \rangle \equiv \int_{y_1}^{y_2} \int_{x_1}^{x_2} \dots \, dx \, dy; \\ \langle \dots \rangle &\equiv \int_{y_1}^{y_2} \dots \, dy; \quad \langle \dots \rangle_x \equiv \int_{x_1}^{x_2} \dots \, dx; \\ \delta_x f(x,y) &\equiv f(x_2) - f(x_1); \quad \text{and } \delta_y f(x,y) \equiv f(y_2) - f(y_1), \end{aligned}$$

The terms in Eq. (1) domain area-averaged transport momentum budgets were estimated for both the *Inner* and *Outer Zones* (defined in Fig. 7) using region-specific algorithms and 5-constituent tidal hindcast time series of (a) observed current time series and (b) $model_{01}$ bottom pressure gradients (PG) at the observation and corresponding model stations in Fig. 4. The horizontal bottom stress was estimated using the same quadratic bottom stress algorithm as used by the QUODDY model. See Appendix B for details of that estimate as well as that for lateral stress.

While ideally the theoretical momentum budget equations (1) sum to zero, our estimates of the momentum budget component equations (presented below) do not. This is because (a) some physics has been disregarded (e.g., stratification-related terms); (b) the estimation algorithms are only approximate; and (c) the observation data used to evaluate the algorithms has uncertainty.

Thus we define residual terms (RES_X and RES_Y), which are sums of the left hand side (LHS) terms Eq. (1); and such that when moved to the LHS close the momentum budgets exactly.

The momentum budgets were estimated from the hindcast observed currents and $model_{01}$ pressure gradients for the Inner and Outer zones. The depth-averaged M_2 tidal current major/minor ellipse characteristics are depicted in Fig. 13. Note that the M_2 tidal current flows, including the zonal average currents, are nearly rectilinear throughout the study region – an indication of the bathymetric influence. By contrast, the $model_{01}$ pressure gradient vector ellipses (see Appendix A for details) are more nearly circular.

(1) Inner zone momentum budget: Observations

The terms in Eq. (1) volume-averaged momentum budget components for the *Inner Zone* (IZ) were estimated according to Appendix B – Table B3 algorithms; which were evaluated using the 5-constituent tidal hindcast time series for a 25-h (\sim lunar day) in 27–28 January 2009 (see Fig. 14 and Table 7/OBS-1). Clearly the $model_{01}$ -derived local pressure gradient terms (PG_Y/PG_X – strongly influenced by the larger-scale western GoM pressure gradients) are prominent in both

momentum components. Dynamically they have different respective roles in these components as discussed next.

IZ Y-momentum (Fig. 14-lower): The pressure gradient term PG_Y and the inertial term ($INER_Y$ – local acceleration) are in approximate balance in supporting a near-standing wave dynamics. The departure from classical standing wave physics is due to a second order modulation by the bottom stress (BSF_Y). The BSF_Y , an even smaller Coriolis (COR_Y), and nonlinear advective acceleration (ADV_Y) terms are almost in quadrature with the primary $PG_Y/INER_Y$ balance. [Note: The estimated lateral stress term is not indicated in Fig. 14 because it is another two orders of magnitude smaller – see Table 7]. The momentum budget is closed by the $-RES_Y$ term, which is about 12% of the total variance of the estimated Y momentum terms. $-RES_Y$ is nearly in anti-phase with PG_Y – suggesting source errors in the pressure-related forcing.

IZ X-momentum (Fig. 14-upper): The primary role of the pressure gradient term PG_X is to turn the primary V flow through the sharp ACW turns at the southern and northern extremes of the tidal ellipse (i.e., at V_{min} at 1800 GMT; at V_{max} at 2312 GMT), respectively. Note that at these turning points PG_X overwhelms and opposing maximum amplitude COR_X , which is a factor of 2 weaker. The only other significant term in the X-component is $-RES_X$ term, which is about 15% of the total variance of the estimated X-terms. $-RES_X$ is nearly in anti-phase with PG_X – also suggesting source errors in the pressure-related forcing.

(2) Outer zone momentum budget: Observations

OZ Y-momentum (Fig. 15-lower): The OZ Y-pressure gradient term PG_Y – dictated by the larger scale regional tidal dynamics – is stronger than its IZ counterpart. This relatively stronger OZ PG_Y term nearly balances a more robust OZ inertial term $INER_Y$ – consistent with standing wave dynamics. OZ $INER_Y$ and other OZ current-related terms (e.g., BSF_Y) are larger than their IZ counterparts simply because there is more momentum in the deeper OZ volume-integrated currents than in the shallower IZ. There is a secondary force balance between the

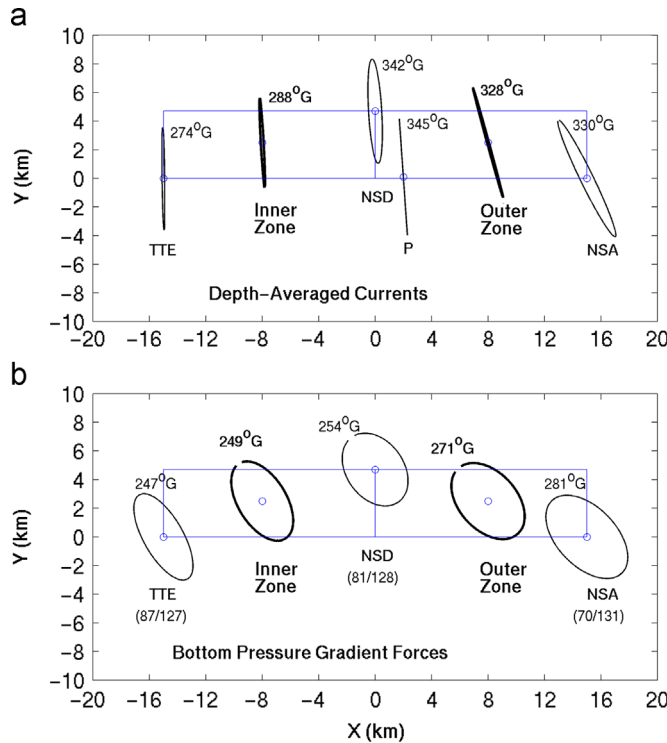


Fig. 13. (a) The observed M_2 tidal cycle water parcel displacement trajectories (derived from progressive vector diagrams) at observation stations of TTE, NSD, and NSA; and at the derived stations P, Inner Zone, and Outer Zone. The station TTE, NSD, and *Inner Zone* water parcels trace anticlockwise (ACW) trajectories, while NSA and *Outer Zone* trajectories are clockwise (CW). The P current vector trajectory (interpolated from the ACW NSD and CW NSB) is rectilinear. The locations of the ellipse centers are located to scale within the greater study region defined by the rectangle. (b) The ellipses for the $model_{01}$ M_2 tidal pressure gradient force vectors (all ACW) at stations. For reference, we also include the M_2 harmonic amplitudes and Greenwich epoch phases of the $model_{01}$ local bottom pressures. Upward is toward $30^\circ T$.

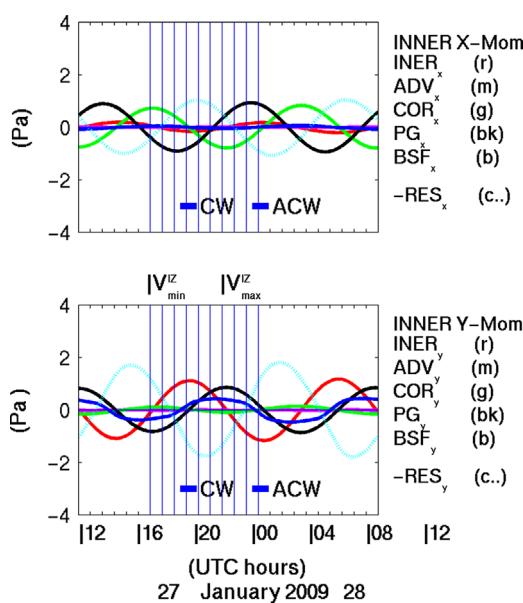


Fig. 14. Estimates of the *Inner Zone* momentum budget (upper) X- and (lower) Y-component terms are based on tidal hindcasts of the *observations* and $model_{01}$ bottom pressure gradients. The ($-RES$) terms close their respective component momentum budgets. The times of the Inner/outer Zone V_{max} and V_{min} and the timing of the generation of clockwise (CW) and anticlockwise (ACW) eddy motion are indicated.

Table 7

Statistics of the *observation*- (*OBS*) and *model-based* (*MOD*) momentum term time series for the X and Y components of several cases employing $model_{01}$ BPs and $C_d=0.01$ for bottom stress. The percentages of the residual (RES) variance relative to that of total of the estimated LHS Eq. (1) term variances are given.

Momentum budget terms	IZ OBS-1 [Fig. 14]		OZ OBS-2 [Fig. 15]		OZ MOD-1 [Fig. 16]	
	SD (Pa)	VAR (Pa ²)	SD (Pa)	VAR (Pa ²)	SD (Pa)	VAR (Pa ²)
INNER-Y						
Inertial	0.80	0.64	1.39	1.92	1.58	2.50
Nonlinear advection	0.07	0.00	0.08	0.00	0.10	0.00
Coriolis	0.09	0.01	0.34	0.12	0.53	0.29
PGF	1.09	1.18	1.54	2.37	1.54	2.37
Bottom stress	0.33	0.11	0.36	0.13	0.67	0.44
Lateral stress	0.00	0.00	0.00	0.00	0.00	0.00
Total LHS variance	1.94		4.54		5.60	
RES_y	0.45	0.21	0.50	0.25	0.32	0.10
		10.8%		5.5%		1.8%
INNER-X						
Inertial	0.13	0.02	0.50	0.25	0.77	0.59
Nonlinear advection	0.01	0.00	0.02	0.00	0.00	0.00
Coriolis	0.56	0.31	0.96	0.92	1.10	1.21
PGF	0.91	0.82	1.50	2.26	1.50	2.26
Bottom stress	0.04	0.00	0.14	0.02	0.33	0.11
Lateral stress	0.00	0.00	0.00	0.00	—	—
Total LHS variance	1.15		3.45		4.17	
RES_x	0.42	0.18	0.48	0.23	0.10	0.01
		15.6%		6.7%		0.2%

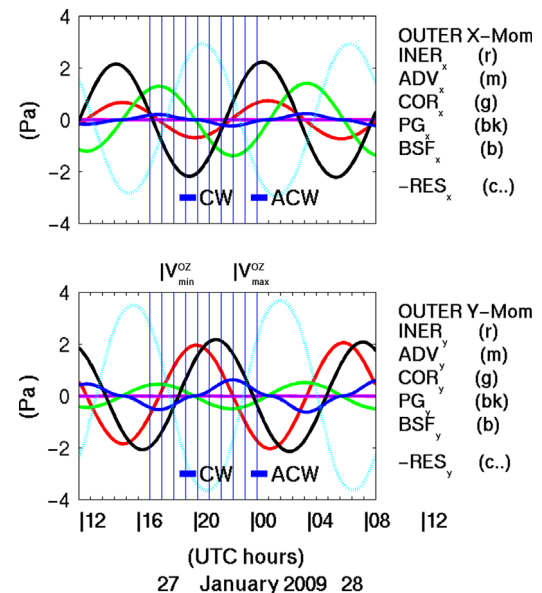


Fig. 15. Estimates of the *Outer Zone* momentum budget (upper) X- and (lower) Y-component terms are based on tidal hindcasts of the *observations* and $model_{01}$ bottom pressure gradients. The ($-RES$) terms close their respective component momentum budgets. The ($-RES$) terms close their respective component momentum budgets. The times of the Inner/outer Zone V_{max} and V_{min} and the timing of the generation of clockwise (CW) and anticlockwise (ACW) eddy motion are indicated.

COR_y and BSF_y terms, which is in quadrature or 90° (3.1 h) out of phase with the primary balance. The residual $-RES_y$ or error term is of secondary amplitude ($\sim 6\%$ of the sum of or total term variances) like COR_y and BSF_y ; and like them peaks in the vicinity of V_{min}^{OZ} and V_{max}^{OZ} – suggesting errors in the estimated bottom stress.

OZ X-momentum (Fig. 15-upper): The primary terms – a robust PG_x and COR_x – are in opposition, but misaligned.

This misalignment is the key to a force balance, where COR_x turns the primary V flow clockwise through the turns at the V_{\min}/V_{\max} extremes of the tidal current ellipse. Like with the OZ Y-momentum, the secondary amplitude $-RES_x$ term ($\sim 7\%$ of the total term variances), is nearly in anti-phase with PG_x – also suggesting source errors in the pressure-related forcing.

(3) Outer zone momentum budget: Model

Finally we compare the *Outer Zone observation-based* momentum budget estimates with their $model_{01}$ -based counterparts. Because the two sets of momentum budget results have the same bottom pressure forcing, it is not surprising that they are quite consistent, with minor differences. For example, the $model_{01}$ -based inertial terms are slightly larger than their observation-based OZ counterpart due to their slightly stronger currents. The latter also contribute to the larger $model_{01}$ BSF_y , although errors in the 55% rule observed bottom currents may also contribute. Still the similarities in Figs. 15 and 16 results are encouraging.

The basic structure of the 100% model-derived OZ momentum budget estimates (Fig. 16; Table 7 MOD-1) based on the same pressure gradient forcing and algorithms is the same as the OZ observation-derived counterparts. The basic exceptions are the near-zero (only a few percent) model-derived $-RES$ s (see Table 7 MOD-1). Now because the model station “data” is by definition internally consistent with the PG forcing, we might expect perfect balances and exactly zero $-RES$ s. However, our estimation algorithms are not perfect. Therefore the non-zero $-RES$ s in this calculation are a quantitative measure of those imperfections; and thus a help in interpreting the $-RES$ s in the observation-derived estimations.

In principle, since the model is dynamically self-consistent, the momentum budget based solely on model results should yield no RES term – that is if the estimation algorithms were perfect. Of course they are not. Thus the residual terms in the model-based momentum budgets are a quantitative measure of the inaccuracies in our approximate momentum budget Eq. (1).

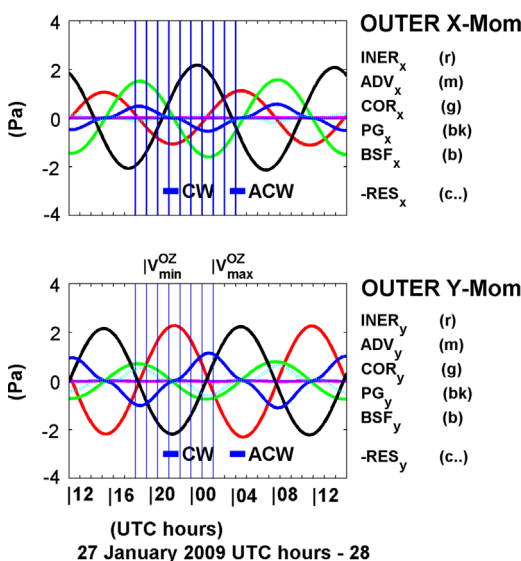


Fig. 16. Estimates of the Outer Zone momentum budget terms in Eq. (1) are based on tidal hindcasts of $model_{01}$ results for the (upper) X and (lower) Y directions, respectively. The $(-RES)$ terms balance their respective component momentum budgets. The times of the Inner/outer Zone V_{\max} and V_{\min} and the timing of the generation of clockwise (CW) and anticlockwise (ACW) eddy motion are indicated.

6.2. Transport vorticity budgets

Following Park and Wang (2000), we consider the conservation of the spatially averaged transport vorticity for the *Inner* and *Outer Zones*. In the configuration considered, the time rate change of transport vorticity is on the same side of the equation as all of the production and dissipation terms – except for the of transport vorticity diffusion which we have difficulty estimating with the available observations:

$$\begin{aligned} \frac{\partial}{\partial t} \langle \Pi \rangle + \frac{1}{A} \left\langle \left(\frac{\partial \bar{U}}{\partial x^2} + \frac{\partial \bar{V}}{\partial x \partial y} - \frac{\partial \bar{U}}{\partial x \partial y} - \frac{\partial \bar{V}}{\partial y^2} \right) \right\rangle + \frac{g}{A} \left\langle \left(\frac{\partial H}{\partial x} \frac{\partial \eta}{\partial y} - \frac{\partial H}{\partial y} \frac{\partial \eta}{\partial x} \right) \right\rangle \\ - \frac{f}{A} \left\langle \frac{\partial \eta}{\partial t} \right\rangle + \frac{1}{A} \left\langle \left[C_d \left| \vec{V}^b \right| \omega^b + C_d \left(\vec{V}^b \times \nabla \left| \vec{V}^b \right| \bullet \vec{k} \right) \right] \right\rangle \\ = \frac{1}{A \rho_o} \left\langle \left(\frac{\partial HT_y}{\partial x^2} - \frac{\partial HT_x}{\partial y^2} \right) \right\rangle \end{aligned} \quad (2)$$

where $\Pi = \partial V / \partial x - \partial U / \partial y$ is the transport vorticity, U and V are horizontal transport components, ρ_o is the reference water density, and $\eta = -(pb/\rho_o g)$ is the sea surface fluctuation in terms of bottom pressure.

Physically the local rate change of the transport vorticity production – term (a) in Eq. (2) transport vorticity budget – is influenced by mechanisms represented by terms:

- (b) nonlinear advection of transport vorticity;
- (c) topographic transport vorticity tendency;
- (d) sea surface divergence;
- (e) bottom stress-induced transport vorticity production/dissipation via:
 - (e1) bottom drag dissipation;
 - (e2) bottom current shear; and
- (f) diffusion of transport vorticity.

All of these terms, except the transport vorticity lateral diffusion term (f), have been estimated for the both zones according to algorithms like those given in Appendix C Table C1 for the Inner Zone (see Fig. 17). The *Inner Zone* time rate change of transport vorticity (LTV) variability transport vorticity time series is the largest is mostly “explained” by the $-RES$ term variability. As with the momentum budget, the $-RES$ term is the negative residual is the sum of all of the estimates of the LHS terms of Eq. (2) and closes the transport vorticity budget exactly.

The $model_{01}$ vorticity maps in Fig. 18 strongly suggest that the transport vorticity diffusion is the most important source of vorticity in the *Inner Zone*. In particular these maps show that (a) around 1540 UTC on 27 January a patch of negative vorticity began to form along the coast just north of our study region. (Note that this occurs as the ACW eddy motion formed earlier separates from the coast); and (b) between 1540 and 1800 UTC the negative vorticity patch grew southward into the *Inner Zone* of our study region – consistent with the Fig. 17 IZ LTV. With the elimination of the positive TV near-shore, the continued diffusion (inflow) of $-TV$ seeds the CW eddy motion formation process for the next 2.5 h. Then at about 2050 UTC, the CBL flow separates from the coast. The $-TV$ signature associated with the seaward translating CW eddy motion is clearly seen at 2204 UTC in Fig. 18. In the same picture we see the initial up-coast patch of positive vorticity, which will feed the future ACW eddy motion.

7. Discussion

The body of evidence presented here suggests a process in which a forced tidal vorticity wave originates in shallow water

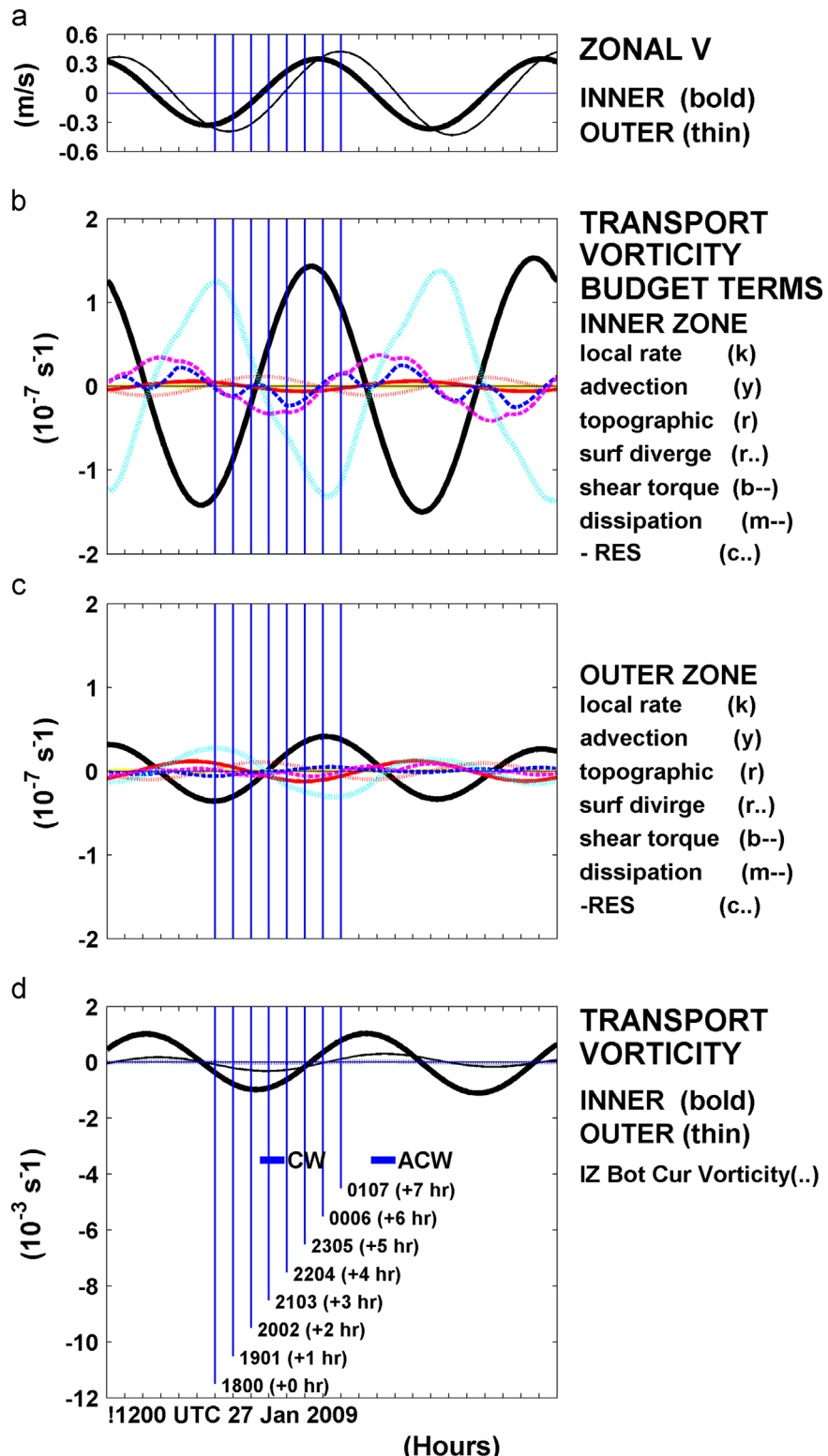


Fig. 17. Transport vorticity budget terms including those for local time-rate change (local rate), nonlinear advection, topographic production tendency, sea surface divergence (surf div), bottom current shear torque, dissipation via bottom drag, and the residual (RES) or sum of the other terms such that $-RES$ closes the budget by definition; for the (b) Inner Zone (IZ) and (c) Outer Zone (OZ). For reference (d) the IZ and OZ transport vorticity and (a) zonal v velocity time series are given; as are the hourly time horizons during with CW and ACW eddy motion formation.

and then propagates across the GSC as either a CW ebb phase eddy motion or ACW flood phase eddy motion – communicating information about the change from ebb-to-flood and flood-to-ebb tidal flows, respectively. The CW (or ACW) eddy motion formation process begins in the shallow water just offshore from Chatham,

MA shortly after maximum ebb (or flood) flow in the GSC. At that time, a growing adverse along-coast pressure gradient force begins to slow the prevailing tidal flow. During the next 2.5 h the vorticity and small-scale eddy motion grows within a coastal boundary layer (CBL) envelop. The CBL then separates from the

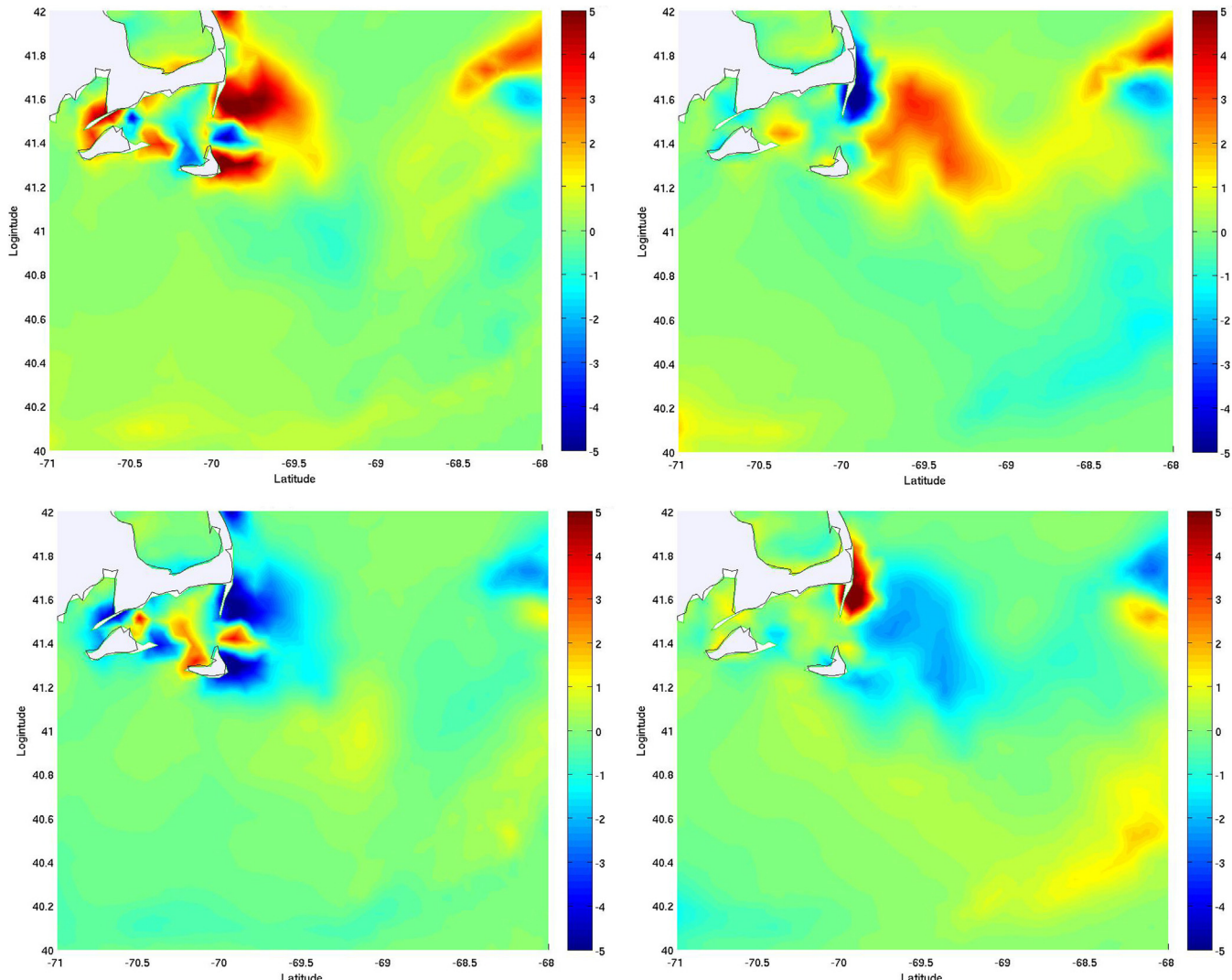


Fig. 18. Model vorticity of depth averaged velocities at the indicated times. (above left) EBB_{full}-2.33 h (1540 GMT 27 January 2009); (above right) EBB_{full} (1759 GMT); (below left) FLOOD_{full}-2.33 h (2204 GMT); (below right) FLOOD_{full} (0016 GMT 28 January '09). The vorticity scale in 10^{-5} s^{-1} units is given to the right.

coast and the eddy motion leaves the near-coast study region and rapidly traverses across the GSC completing the change from ebb to flood tidal flow in the GSC region.

We have found that the momentum budgets, in particular, show that the first order dynamics of the study region are standing wave dynamics that are forced by the GoM-scale semidiurnal frequency (primarily M₂) tidal pressure gradients and modulated by local bottom stress. The relative timing of the dominant cross-zonal (Y-direction) dynamical elements of this forced standing wave, including the bottom stress, is depicted in Fig. 19.

We have found that, although bottom stress (BSF) is modest relative to PGF and INER, it is an essential element in the formation of the eddy motion. In fact, an unusually large drag coefficient was needed for the model so that model and observed currents were reasonably consistent. The research of Edwards et al. (2004) and McCabe and MacCready (2006) suggest that in such situations with rough bottom bathymetry and flow separation form drag (caused by unbalanced pressure forces on the flow in the presence of significant bathymetric change) may be significant. Thus it is very likely that our large drag coefficients indicate the importance of form drag in addition to bottom friction in retarding the flow. These unusually strong drag forces in the shallower waters near the coast assist the adverse pressure gradients in slowing the tidal flow in the CBL – leading to separation and

the eddy motion focus of this paper. We next explore the vorticity dynamics of the study region.

We have found that, the *Inner Zone* transport vorticity dynamics is significantly more energetic in the eddy motion formation region than in the *Outer Zone*. The diffusion of negative transport vorticity into the *IZ* from the near coast to the north, augmented by lesser amounts of transport vorticity production by bottom current shear torque and squashing, and muted by bottom drag-induced dissipation – feeds the slow growth of the CW eddy motion between 1800 and 2000 UTC – 27 January 2009. Between 2000 and 2100, the CBL/CW eddy motion separates from the coast; and in the process, the eddy motion expands in lateral scale across the *Outer Zone* (see Fig. 9d), accompanied by a five-fold decrease in transport vorticity diffusion. At the same time, positive transport vorticity is beginning to diffuse from the near coast to the north into the *Inner Zone* – fueling the formation of the ACW flood current eddy motion to come.

Thus it appears that transport vorticity diffusion is the most important source of vorticity supplying negative transport vorticity ($-TV$) in this case CW eddy motion formation. Also contributing lesser amounts of $-TV$ are dissipation, shear torque, and topographic tendency minus surface divergence stretching. Just before 1800 UTC, the *IZ* transport vorticity (TV) transitions from positive to negative (coincident with the LTV minima).

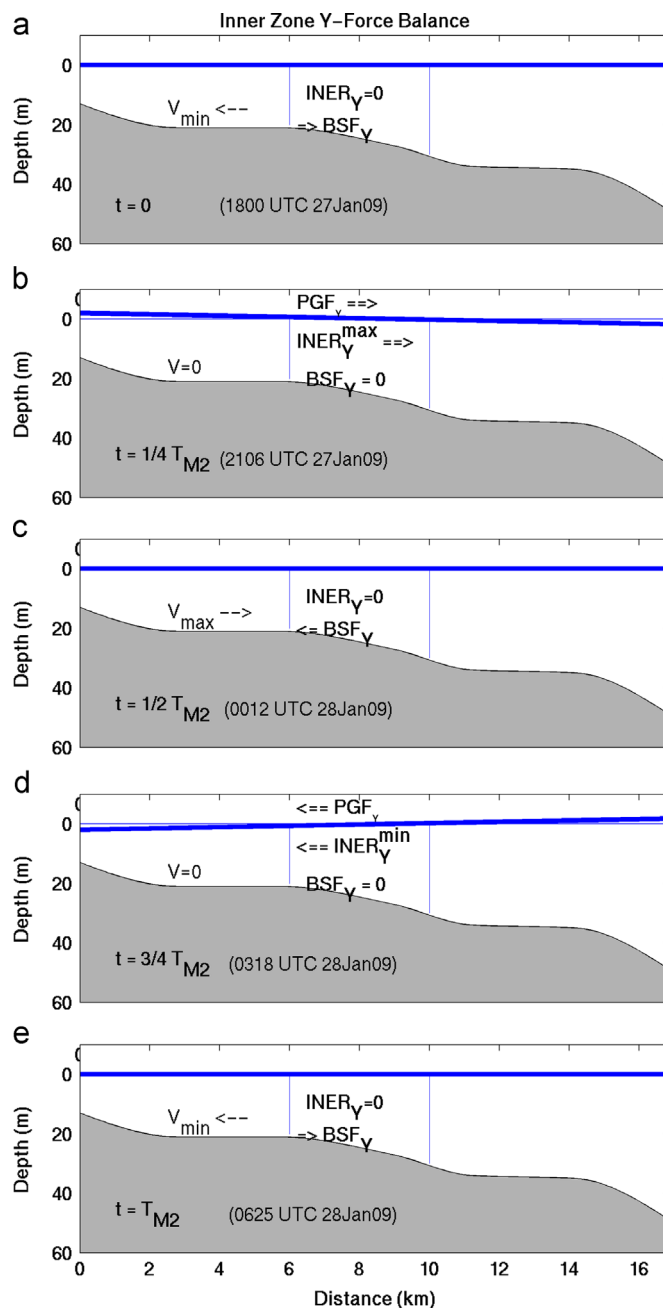


Fig. 19. The forced, drag-mediated standing wave character of the dynamics is illustrated in this sequence of force balance Y - z sections across the Inner Zone. The 5-panel sequence starts with EBB_{full} (i.e., V_{\min}) at 1800 UTC 27 January 2009 depicts each $1/4 M_2$ tidal period through a full cycle. (a) At $t=0$, the bottom stress force BSF_Y is opposing V_{\min} and the sea level tilt-induced pressure gradient force (PGF_Y) is going positive. During the next $1/4 M_2$ period, the increasing PGF_Y slows $-V$ (i.e., accelerates the flow); (b) at $t=1/4 T_{M2}$, $V=0$ coincides with PGF_Y and $INER_Y^{\max}$. During the next $1/4 M_2$ period, a decreasing PGF_Y continues to accelerate V (which is opposed by $-BSF_Y$). (c) At $t=1/2 T_{M2}$, sea level is momentarily flat again (or $PGF_Y=0$) before going negative. During the next $1/4 M_2$ period, a $-PGF_Y$ slows $+V$ flow; (d) at $t=3/4 T_{M2}$, $V=0$ coincides with PGF_Y and $INER_Y^{\min}$. During the final $1/4 M_2$ period of the cycle, a decreasing $-PGF_Y$ continues to accelerate $-V$, which returns to (e) V_{\min} .

This research has addressed a set of specific questions concerning tide-related eddy motion in the western GoM. The following outlines our answers to those questions.

7.1. What are the size and energy ranges of this eddy motion?

Here we have shown that the eddy motion is an integral part of the change between semidiurnal ebb and flood tidal flow in the

Great South Channel in the western Gulf of Maine. Specifically, the eddy motion originates near the Cape Cod coast as 1 cm/s – kilometer-scale patches of accumulating vorticity (CW just after maximum ebb flow; ACW for flood flow). Over the next 2.5 h, the eddy motion velocities increase in intensity and scale to 10 cm/s – 10 km-scale features that separate from the coast. During the final half hour phase of a particular eddy motion (that comes with the completed change of tide), they expand in lateral scale to that of the width of the Great South Channel (order 100 km) and disappear as the primary tidal flow fills the channel at EBB_{max} or FLOOD_{max}.

7.2. What is the role of bottom stress in the formation and evolution of transient tidal eddy motions in the great south channel?

Our study results concerning the kinematics and dynamics of the eddy motion clearly show the dynamical sensitivity of the eddy motion formation process to bottom stress and bottom stress gradients in the near-shore shallow water. Furthermore our results strongly suggest the role of form drag in augmenting and maybe dominating bottom friction in the basic tidal flow dynamics in our shallow water study region. Thus, we conclude from these results that model bottom stress parameterization needs to be more spatially variable than is commonly employed in order to model this transient tidal eddy motion properly.

The GSC eddy motions, with their large translation speeds (~25 m/s) are clearly phase eddies. Black and Gay (1987) have showed analytically that significant bottom friction generates phase eddies in tidal flows. We have shown that, indeed, bottom drag (friction plus implied form drag) is an essential factor in the formation and separation of the CBL envelop in which the eddy motion forms during the accelerating phase of the semidiurnal tidal flow cycle. This is most evident in the magnitude and tidal phase of our measured station TTE currents compared to those at historical stations NSD and NSA.

One of the clearest results of this research was the need to impose much larger drag on the model flows to reconcile them with the observations. That increase in the space-time independent drag from $C_d=0.005$ to $C_d=0.010$ in the model indeed slowed the model tidal currents within our 10–40 m depth near-shore study region. The price for these “improved” $model_{01}$ currents (relative to the observations) – significant differences in the tidal characteristics (relative to $model_{005}$) throughout the rest of the model domain. Thus we conclude that a space-dependent bottom drag is needed in the model to get the correct tidal currents throughout the model domain.

7.3. How are the dynamics of this transient eddy motion related to those of the tidal eddies reported by Geyer and Signell (1990) off of gay head/Martha's Vineyard, MA?

The GSC phase eddy motions differ in important ways from the Geyer and Signell (1990), Martha's Vineyard (MV) eddies which are shed via CBL separation on opposite sides of a promontory during alternating respective ebb and flood tidal flows. The Signell and Geyer (1991) modeling highlights the role of bathymetric change in producing the distinct and relatively slower moving MV eddies. By contrast, our GSC transient tidal CW and ACW eddy motions are phase eddies – akin to the Black and Gay (1987) eddies – ones which translate along the same seaward trajectory signaling the change of tide in the GSC. Clearly CBL separation is common to both, but the bottom stress and bathymetry environments differ. To clarify the distinctions, particularly as it concerns bottom drag/friction, more detail involving both new observations and numerical circulation modeling are required.

7.4. How feasible will it be to routinely measure the GSC eddy motion using HF radar?

The eddy motion has distinctive flow and vorticity signatures relative to the basic forced standing wave response of the study region. The eddy motion signature EMS-1 (Fig. 20b) is defined by subtracting the average Inner Zone average current from the individual station currents. The eddy motion signature EMS-2 (Fig. 20c) is defined by subtracting the average Inner+Outer Zone

average current from the individual station currents. Of course it is not surprising that all of the signature maxima coincide with the presence of both the CW and ACW eddy motions in the study region. Also note that, because the station TTE current is the weakest of all of the station currents, it exhibits the most robust EMS-1 and EMS-2 signatures. Unfortunately, station TTE is so close to the coast that its current is not reliably detected in the HF radar surface current maps. Therefore an eddy motion detection scheme would need to rely on further offshore currents where

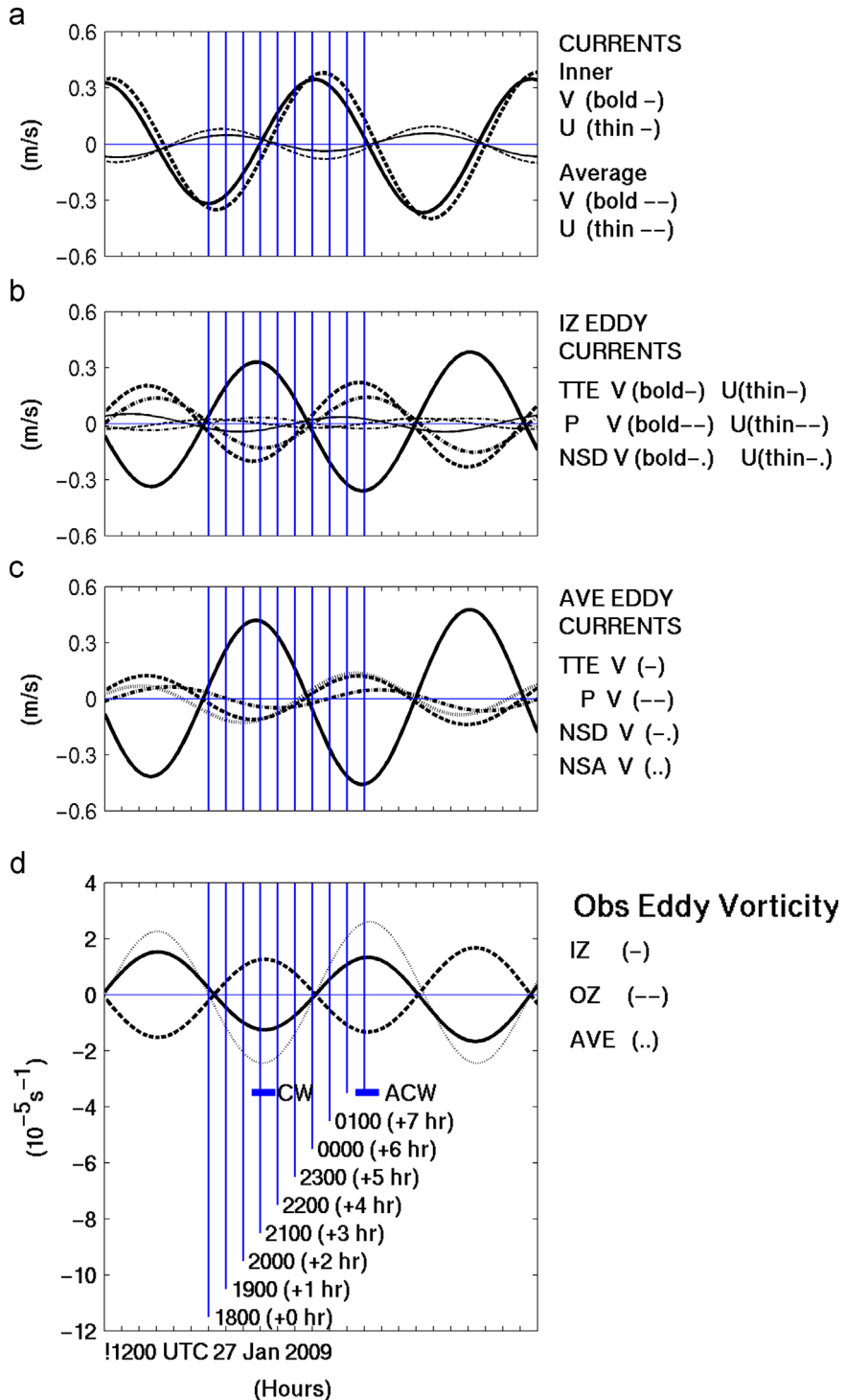


Fig. 20. Eddy motion current signatures, including: (a) observed Inner Zone and Study Region (IZ+OZ)-averaged currents; (b) observed IZ “eddy motion” currents (see text for definitions); (c) observation station eddy motion currents relative to Study Region average current; and (d) observed IZ and OZ eddy motion vorticity relative to Study Region average vorticity. The vertical lines mark the hourly milestones in the flow kinematics (see Table 6), including durations of the CW and ACW eddy motion.

both eddy motion signatures are somewhat weaker depending on how the regional mean current is computed. We are exploring whether or not a better eddy detection scheme might involve surface current vorticity (see Fig. 20d) despite the increased noisiness due to double differencing of current vectors – each with their own uncertainties.

8. Summary of conclusions

Historical Coastal Ocean Dynamics Applications Radar (CODAR) – derived surface current maps of the Great South Channel region of the western Gulf of Maine revealed clockwise (CW) and anticlockwise (ACW) eddy motion about 2.5 h after maximum ebb and flood tidal currents, respectively. To better elucidate the kinematics and dynamics of these transient tidal eddy motions, an observational/modeling program was conducted during the very weakly stratified winter 2008–2009 conditions. Moored measurements of bottom pressure and currents in 13 m of water near Chatham MA were augmented by an array of historical measurements for which we had tidal harmonic constants for the five principal tidal constituents. A homogeneous, high resolution, finite element coastal ocean model (called QUODDY), which was forced with the five principal tidal constituents (M_2 , N_2 , S_2 , K_1 , and O_1), produced 4-dimensional pictures detailing the formation, evolution, and across-GSC translation of alternating ebb and flood flow-forced CW and ACW eddy motions respectively. The principal results of this research are as follows:

- The observed and model time series, which were generated using the appropriate principal tidal constituents, showed that our shallow nearshore study region (10–35 m depth) were dominated by M_2 semidiurnal currents; which typically trace highly polarized ~6 km peak-to-peak elliptical paths in the along-shore northeast–southwest (~30–210°T) direction.
- Observation versus model comparisons prompted us to increase the model bottom drag coefficient from $C_d=0.005$ to 0.010 in order to reconcile current amplitude differences of up to 50% in our shallow study region where the eddy motion formed.
- The observation- and the model-based eddy motion kinematics are consistent with CW or ACW eddy motions that (a) grow nearshore in the coastal boundary layer (CBL) under the influence of an adverse pressure gradient force for about 3 h after the respective ebb or flood current maxima; (b) the CBL separates; and (c) the eddy motion (both CW and ACW) begins translating at speeds of about 25 m/s along a south-eastward trajectory along the curved 50 m isobath across the GSC.
- A first order, forced standing tidal wave dynamics was revealed in the cross-isobath momentum budget estimates in both an *Inner Zone* (average depth 23 m) and an *Outer Zone* (average depth 33 m). The principal force balance between the pressure gradient and inertial terms was modulated by the weaker (i.e., second order) bottom stress and Coriolis forces; which were somewhat stronger in the stronger flow *Outer Zone*. The observation and model-based momentum budget estimates in *Outer Zone* compared well.
- *Inner Zone* transport vorticity budget estimates reveal the dominant role of vorticity diffusion, supported by lesser bottom shear stress and water column stretching/squashing in modulating the eddy motion vorticity.
- It appears that it will be feasible to quantify the strength of this eddy motion using HF radar-derived surface currents; and thus study the effects of stratification, winds and other

oceanographic processes on the metronome-like transient tidal eddies in the western Great South Channel.

Acknowledgments

This research benefitted from implementation of high frequency radar to measure surface currents led by Zhitao Yu, with timely assistance from Josh Kohut. We gratefully acknowledge the cooperation and support of the US National Park Service, who provides space and infrastructure support for the CODAR instrumentation at their Cape Cod National Seashore station at Eastham, MA – near Nauset, MA. We also have benefitted greatly from Zhitao Yu's earlier implementation of the QUODDY numerical model for this research. This publication is the result in part of research sponsored by The MIT Sea Grant College Program, under NOAA Grant Number NA06OAR4170019, MIT SG Project Number 2007-R/RC-104. This research has also been supported in part through a subcontract to Rutgers University who is the prime funded under NOAA grant NA07NOS4730221 for the implementation of the Mid Atlantic Regional Association Coastal Ocean Observing System (MARACOOS).

Appendix A. Selected observed and model pressure and current harmonic constants

A.1. Observed tidal pressures and currents

The tidal harmonic constants in Table A1 were derived from a harmonic analysis of our measured moored bottom pressure record at a depth of 13 m depth at station TTE off of Chatham, MA. The harmonic constants for a historical bottom pressure record from a depth of 7 m off of Nauset, MA. The results from both of these analyses show that the regional tidal sea level variability is clearly dominated by the M_2 semidiurnal tides.

The harmonic analysis results of the station TTE observed (ADCP) current series (Table A2) are also clearly dominated by the M_2 semidiurnal tidal variability.

Appendix B. Eddy motion momentum conservation

The momentum and vorticity budgets are estimated using the algorithms and approximations described below for the *Inner* and *OZs* in the rotated (30° clockwise) coordinate system; as defined in Fig. 7. The basis for this analysis is as follows.

Table A1

The principal tidal harmonic constants for the *observed* station TTE (depth 13 m) bottom pressures (BP) in terms of amplitudes (decibars) and Greenwich epoch phases. The TTE five principal plus two nonlinear tidal constituent harmonic constants, with estimated uncertainties, are based on the analysis of the 57-day record (3 November to 30 December 2008); and compared with the Moody et al. (1984) harmonic constants for the historical BP measurements off of Nauset, MA (NAU; 7 m depth).

Con	TTE Amp (db)	TTE Phase (°G)	NAU Amp (db)	NAU Phase (°G)
M_2	1.103 ± 0.013	119 ± 1	1.032	102
N_2	0.238 ± 0.013	96 ± 3	0.222	70
S_2	0.170 ± 0.013	156 ± 4	0.144	133
K_1	0.132 ± 0.013	192 ± 6	0.131	201
O_1	0.114 ± 0.013	209 ± 5	0.115	182
M_4	0.027	16	–	–
M_6	0.030	178	–	–

Table A2

The tidal harmonic constants for the five principal and two nonlinear constituents of the moored station TTE eastward and northward currents at 6 m and 8 m AB between 3 November and 29 December 2008 (56 day) in terms of amplitude and Greenwich epoch phases. Current ellipses are given in terms of major axis amplitude and orientation, ellipticity (ε =major/minor; positive major axis amplitude indicates an anticlockwise rotating current vector); and the Greenwich phase of the maximum current.

Depth	Tidal Const	Total Var (cm/s) ²	East Amp (cm/s)	Phase (°G)	North Amp (cm/s)	Phase (°G)	Major Axis Amp (cm/s)	Maj Axis Dir (°T)	ε	V _{max} (°G)
6 m	M ₂	1960	21.2 ± 0.5	272 ± 1	38.8 ± 1.1	275 ± 1	44.3	29	37	274
	N ₂	62	3.7 ± 0.5	244 ± 7	6.7 ± 1.1	252 ± 9	7.7	29	19	250
	S ₂	61	2.1 ± 0.5	312 ± 12	6.4 ± 1.1	313 ± 7	6.7	18	∞	313
	K ₁	3	0.9 ± 0.5	302 ± 35	1.5 ± 1.1	260 ± 39	1.6	25	-3	270
	O ₁	0	0.2 ± 0.4	324 ± 75	0.1 ± 0.1	241 ± 106	0.4	88	∞	324
	M ₄	6	1.1	146	2.3	116	2.6	21	4	170
	M ₆	1	0.8	16	0.8	296	1.1	56	11	21
8 m	M ₂	2185	23.0 ± 0.5	272 ± 1	40.7 ± 1.1	275 ± 1	46.7	30	42	274
	N ₂	67	3.9 ± 0.5	244 ± 7	7.0 ± 1.1	252 ± 9	8.0	29	16	251
	S ₂	65	2.1 ± 0.5	312 ± 12	6.7 ± 1.1	312 ± 7	7.0	17	∞	313
	K ₁	3	0.9 ± 0.5	296 ± 35	1.7 ± 1.1	260 ± 39	1.9	25	-4	268
	O ₁	0	0.2 ± 0.4	335 ± 75	0.1 ± 0.1	129 ± 106	0.2	282	∞	334
	M ₄	5	1.0	139	2.2	116	2.3	21	4	170
	M ₆	1	0.9	18	0.6	296	1.1	56	11	21

The vector form of the momentum equations is

$$\frac{D\vec{u}}{Dt} = \frac{\partial \vec{u}}{\partial t} + \vec{u} \cdot \nabla \vec{u} - \vec{f} \times \vec{u} = -\frac{1}{\rho} \nabla p + \frac{1}{\rho} [\nabla \cdot \vec{\sigma}], \quad (\text{B.1})$$

where $\vec{u} = u \vec{i} + v \vec{j} + w \vec{k}$ is the total velocity; f is the Coriolis parameter, ρ =water density, p is pressure, and $\vec{\sigma}$ is the stress tensor.

Following the Brown (1984) application to external tidal variability on Georges Bank, the continuity relation:

$$\frac{\partial u}{\partial x} + \frac{\partial v}{\partial y} + \frac{\partial w}{\partial z} = 0 \quad (\text{B.2})$$

is vertically integrated between the local bottom at $z=-h$ (x, y) (rel. mean sea level at $z=0$) and the sea surface at $z=\eta$ (x, y, t) resulting in

$$\frac{\partial(\eta+h)}{\partial t} + \frac{\partial U}{\partial x} + \frac{\partial V}{\partial y} = 0, \quad (\text{B.3})$$

where U and V are local volume transports and $\eta+h=H$ – the total instantaneous water column height. Thus the vertically averaged currents are related to the transports by

$$V/H = \bar{u}, \dots, V/H = \bar{v}.$$

For reasonably long waves with tidal and subtidal frequencies, the vertical momentum equation reduces to the hydrostatic balance $\partial p/\partial z = -\rho g$, which when integrated vertically from an arbitrary elevation z to mean sea level at $z=0$ leads to

$$\hat{p}(z) = \hat{p}(0) + g \int_z^0 \rho dz. \quad (\text{B.4a})$$

The near-surface pressure can be written as

$$\hat{p}(0) = p_a + \rho_s g \eta, \quad (\text{B.4b})$$

where p_a is atmospheric pressure and ρ_s is the near surface density $\rho(0)$. Partitioning density to a reference density ρ_0 and a small departure ρ' according to

$$\rho = \rho_0 + \rho'(x, y, z, t)$$

allows us to write Eq. (B.4) as

$$\hat{p}(z) = p_a + \rho_s g \eta + \rho_0 g z + g \int_z^0 \rho dz. \quad (\text{B.5a})$$

For dynamical considerations we need only to consider departures from the hydrostatic or motionless state and thus we partition the pressure as $p(x, y, z, t) = p^\wedge(x, y, z, t) + \rho_0 g z$, which allows us to write Eq. (B.5a) as

$$\frac{p(z)}{\rho_0} = \frac{p_a}{\rho_0} + \frac{p_s}{\rho_0} g \eta + \frac{g}{\rho_0} \int_z^0 \rho' dz, \quad (\text{B.5b})$$

which when evaluated at $z=-h$, becomes the perturbation bottom pressure:

$$\frac{p_b}{\rho_0} = \frac{p(z=-h)}{\rho_0} = \frac{p_a}{\rho_0} + \frac{p_s}{\rho_0} g \eta + \frac{g}{\rho_0} \int_{-h}^0 \rho' dz. \quad (\text{B.5c})$$

Returning to the momentum equations, we first multiply the continuity Eq. (B.2) by u and then a second time by v and insert those results into the appropriate components of Eq. (B.1). The following results

X-direction

$$\frac{\partial u}{\partial t} + \frac{\partial u^2}{\partial x} + \frac{\partial u v}{\partial y} + \frac{\partial u w}{\partial z} - f v = -\frac{1}{\rho} \frac{\partial \hat{p}}{\partial x} + \frac{1}{\rho} \left(\frac{\partial \sigma_{xx}}{\partial x} + \frac{\partial \tau_{yx}}{\partial y} + \frac{\partial \tau_{zx}}{\partial z} \right). \quad (\text{B.6a})$$

Y-direction

$$\frac{\partial v}{\partial t} + \frac{\partial u w}{\partial x} + \frac{\partial v^2}{\partial y} + \frac{\partial u v}{\partial z} + f u = -\frac{1}{\rho} \frac{\partial \hat{p}}{\partial y} + \frac{1}{\rho} \left(\frac{\partial \tau_{xy}}{\partial x} + \frac{\partial \sigma_{yy}}{\partial y} + \frac{\partial \tau_{zy}}{\partial z} \right). \quad (\text{B.6b})$$

Assuming a homogeneous ocean at $\rho=\rho_0$, we vertically integrate the momentum Eqs. (B.6), with the liberal use Leibnitz's rule and Eq. (B.3), leads to

X-direction

$$\frac{\partial U}{\partial t} + \frac{\partial \bar{u} U}{\partial x} + \frac{\partial \bar{v} U}{\partial y} - f V = -\frac{H}{\rho_0} \frac{\partial p_b}{\partial x} + \frac{1}{\rho_0} \left[(\tau_x^s - \tau_x^b) + \alpha \right], \quad (\text{B.7a})$$

Y-direction

$$\frac{\partial V}{\partial t} + \frac{\partial \bar{u} V}{\partial x} + \frac{\partial \bar{v} V}{\partial y} + f U = -\frac{H}{\rho_0} \frac{\partial p_b}{\partial y} + \frac{1}{\rho_0} \left[(\tau_y^s - \tau_y^b) + \beta \right], \quad (\text{B.7b})$$

where surface and bottom stresses are τ^s/τ^b and the lateral stresses are

$$\alpha = \frac{\partial h T_x}{\partial x} + \frac{\partial \bar{v} T_x}{\partial y} \quad \text{and} \quad \beta = \frac{\partial h T_y}{\partial x} + \frac{\partial \bar{v} T_y}{\partial y}. \quad (\text{B.7c})$$

We now laterally integrate Eqs. (B.7) over our study region to obtain in the
X-direction

$$\frac{\rho_o}{A} \left\{ \frac{\delta \langle U \rangle}{\delta t} + \langle \delta_x \bar{u} U \rangle_y + \langle \delta_y \bar{v} U \rangle_x - f \langle V \rangle + \frac{1}{\rho_o} \left\langle H \frac{\partial p_b}{\partial x} \right\rangle - \frac{1}{\rho_o} \left\langle \tau_x^s - \tau_x^b \right\rangle - \frac{1}{\rho_o} \left\langle \frac{\partial h T_x}{\partial x} + \frac{\partial h T_x}{\partial y} \right\rangle \right\} = 0 \quad (\text{B.8a})$$

inertial nonlinear Coriolis pressure gradient horizontal stress lateral stress

Y-direction

$$\frac{\rho_o}{A} \left\{ \frac{\delta \langle V \rangle}{\delta t} + \langle \delta_x \bar{u} V \rangle_y + \langle \delta_y \bar{v} V \rangle_x + f \langle U \rangle + \frac{1}{\rho_o} \left\langle H \frac{\partial p_b}{\partial y} \right\rangle - \frac{1}{\rho_o} \left\langle \tau_y^s - \tau_y^b \right\rangle - \frac{1}{\rho_o} \left\langle \frac{\partial h T_y}{\partial x} + \frac{\partial h T_y}{\partial y} \right\rangle \right\} = 0, \quad (\text{B.8b})$$

where the domain area is $A = \Delta x \Delta y = (x_2 - x_1)(y_2 - y_1)$, ρ_o is the reference water density, p_b is bottom pressure, τ^s and τ^b are surface and bottom stress respectively. The notation for the different integral and difference operators are

$$\begin{aligned} \dots &\equiv \frac{1}{H} \int_{-h}^n \dots dz; \quad [\dots] \equiv \int_{y_1}^{y_2} \int_{x_1}^{x_2} \int_{-h}^n \dots dx dy dz; \\ \langle \dots \rangle &\equiv \int_{y_1}^{y_2} \int_{x_1}^{x_2} \dots dx dy; \\ \langle \dots \rangle_y &\equiv \int_{y_1}^{y_2} \dots dy \quad \langle \dots \rangle_x \equiv \int_{x_1}^{x_2} \dots dx \quad \delta_x f(x, y) = f(x_2) - f(x_1) \end{aligned}$$

For this study, with the surface stress τ^s , $\partial h T_x / \partial x \dots$ and... $\partial h T_y / \partial y$ assumed to be negligible, Eq. (B.8) becomes in the X-direction

$$\frac{\rho_o}{A} \left\{ \frac{\delta \langle U \rangle}{\delta t} + \langle \delta_x \bar{u} U \rangle_y + \langle \delta_y \bar{v} U \rangle_x - f \langle V \rangle + \frac{1}{\rho_o} \left\langle H \frac{\partial p_b}{\partial x} \right\rangle + \frac{1}{\rho_o} \left\langle \tau_x^b \right\rangle - \frac{1}{\rho_o} \left\langle \delta_y h T_x \right\rangle_x \right\} = 0, \quad (\text{B.9a})$$

inertial nonlinear Coriolis pressure gradient horizontal stress lateral stress

Y-direction

$$\frac{\rho_o}{A} \left\{ \frac{\delta \langle V \rangle}{\delta t} + \langle \delta_x \bar{u} V \rangle_y + \langle \delta_y \bar{v} V \rangle_x + f \langle U \rangle + \frac{1}{\rho_o} \left\langle H \frac{\partial p_b}{\partial y} \right\rangle + \frac{1}{\rho_o} \left\langle \tau_y^b \right\rangle - \frac{1}{\rho_o} \left\langle \delta_x h T_y \right\rangle_y \right\} = 0. \quad (\text{B.9b})$$

Table B1

Inner zone: A summary of the algorithms and corresponding assumptions used to estimate Eq. (B.2) volume-integrated momentum budget terms (units N/m²=Pa) using rotated observed hindcast series with subscripts referenced to the stations IDs in Fig. 8; with $\Delta x = 15.47$; $\Delta y = 4.17$ km; the = 13 m; $h_p = 30$ m; $h_D = 33$ m; and $h_A = 33$ m.

Data	Term	Estimate algorithm	Assumptions
INER _x	$\frac{\rho_o}{A} \frac{\delta \langle U \rangle}{\delta t}$	$(\rho_o/2) \frac{\delta}{\delta t} (\bar{u}_P + \bar{u}_{TE})$	Linear var. of velocity $\rho_o = 1025.7 \text{ kg m}^{-3}$
INER _y	$\frac{\rho_o}{A} \frac{\delta \langle V \rangle}{\delta t}$	$(\rho_o/2) \frac{\delta}{\delta t} (\bar{v}_P + \bar{v}_{TE})$	Linear var. of velocity
COR _x	$\frac{\rho_o f}{A} \langle V \rangle$	$-(\rho_o f/2) (\bar{v}_P + \bar{v}_{TE})$	$\rho_o f = 0.099 \text{ kg s}^{-1} \text{ m}^{-3}$
COR _y	$\frac{\rho_o f}{A} \langle U \rangle$	$(\rho_o f/2) (\bar{u}_P + \bar{u}_{TE})$	
NonLinA _x	$\frac{\rho_o}{A} \langle \delta_x \bar{u} U \rangle_y$	$\frac{\rho_o}{\Delta x} [(\bar{u}_P U_P/h_P) - (\bar{u}_{TE} U_{TE}/h_{TE})]$	No y-var of $\delta_x \bar{u} U \rho_o / \Delta x h_{TE} = 5.1 \times 10^{-3} \text{ kg m}^{-5}$ $\rho_o / \Delta x h_p = 2.2 \times 10^{-3} \text{ kg m}^{-5}$
NonLinB _x	$\frac{\rho_o}{A} \langle \delta_y \bar{v} U \rangle_x$	$\frac{\rho_o}{\Delta y} [(\bar{v}_D U_D/h_D) - (\bar{v}_P V_P/h_P)]$	No x-var of $\delta_y \bar{v} U \rho_o / \Delta y h_D = 7.5 \times 10^{-3} \text{ kg m}^{-5}$ $\rho_o / \Delta y h_p = 8.2 \times 10^{-3} \text{ kg m}^{-5}$
NonLinA _y	$\frac{\rho_o}{A} \langle \delta_x \bar{u} V \rangle_y$	$\frac{\rho_o}{\Delta x} [(\bar{u}_P V_P/h_P) - (\bar{u}_{TE} V_{TE}/h_{TE})]$	No y-var of $\delta_x \bar{u} V$
NonLinB _y	$\frac{\rho_o}{A} \langle \delta_y \bar{v} V \rangle_x$	$\frac{\rho_o}{\Delta y} [(\bar{v}_D V_D/h_D) - (\bar{v}_P V_P/h_P)]$	No x-var of $\delta_y \bar{v} V$
PresGrad _x	$\frac{\rho_o}{A} \left(\frac{1}{\rho_o} \langle H \partial p_b / \partial x \rangle \right)$	$\{ [h_{TE} (\delta p_b / \delta x)]_{TE} + [h_D (\delta p_b / \delta x)]_D \} \cdot 0.5$	Average($\delta p_b / \delta x$) constant on A
PresGrad _y	$\frac{\rho_o}{A} \left(\frac{1}{\rho_o} \langle H \partial p_b / \partial y \rangle \right)$	$\{ [h_{TE} (\delta p_b / \delta y)]_{TE} + [h_D (\delta p_b / \delta y)]_D \} \cdot 0.5$	Average($\delta p_b / \delta y$) constant on A
BotStress _x	$\left(\frac{1}{A} \langle \tau_x^b \rangle \right)$	$\frac{\rho_o C_d}{2} \left[\left \sqrt{u_{IE}^{bot}}^2 + v_{IE}^{bot}^2 \right u_{TE}^{bot} + \left \sqrt{u_D^{bot}}^2 + v_D^{bot}^2 \right u_D^{bot} \right]$	$C_d = 0.010 \rho_o C_d / 2 = 5.1 \text{ kg/m}^3$
BotStress _y	$\left(\frac{1}{A} \langle \tau_y^b \rangle \right)$	$\frac{\rho_o C_d}{2} \left[\left \sqrt{u_{IE}^{bot}}^2 + v_{IE}^{bot}^2 \right v_{TE}^{bot} + \left \sqrt{u_D^{bot}}^2 + v_D^{bot}^2 \right v_D^{bot} \right]$	
LatStress _x	$\frac{\rho_o}{A} \frac{\delta \langle u \rangle}{\delta t}$	$-(\rho_o v_H / \Delta y^2) (h_D - h_p) [(\bar{v}/h)_D - (\bar{v}/h)_p]$	$v_H = 5 \text{ m}^2 \text{ s}^{-1} \rho_o v_H / \Delta y^2 = 2.95 \times 10^{-4} \text{ kg m}^{-3} \text{ s}^{-1}$
LatStress _y	$\frac{\rho_o f}{A} \langle u \rangle$	$-(\rho_o v_H / \Delta x^2) (h_p - h_{TE}) [(\bar{v}/h)_p - (\bar{v}/h)_D]$	$\rho_o v_H / \Delta x^2 = 2.14 \times 10^{-5} \text{ kg m}^{-3} \text{ s}^{-1}$

Estimating the momentum budget terms: To estimate the terms in Eq. (B.9), we used the 5-constituent tidal hindcasts of the observed current stations located in Table 1; and model₀₁

pressures and currents at stations located in Fig. 7. Eq. (B.9) momentum budget terms were estimated for the Inner Zone using the algorithms and assumptions detailed in Table B1. The stress terms were estimated from algorithms derived as follows.

To be consistent with the QUODDY model, the tidal bottom stress (τ_x^b / τ_y^b) time series were estimated at each station using hindcast bottom currents and the following quadratic bottom stress algorithm:

$$\tau_x^b = \rho_o C_d \left(\sqrt{(u^b)^2 + (v^b)^2} \right) u^b, \quad \tau_y^b = \rho_o C_d \left(\sqrt{(u^b)^2 + (v^b)^2} \right) v^b, \quad (\text{B.10})$$

where $C_d (=0.010)$ is the bottom drag coefficient and u^b / v^b are the near-bottom current components at the station; and $\vec{V}^b = u^b \vec{i} + v^b \vec{j}$ is the bottom current vector.

The model bottom currents were used to estimate the model bottom stress terms. Except for station TTE, near-bottom observed

currents were not available. Alternatively from an inspection of model 21-level current profiles in our study region, we empirically determined a “55% rule” for converting observed mid-depth currents to bottom currents according to:

$$u^b = 0.55 \bullet \bar{u} / h; \quad v^b = 0.55 \bullet \bar{v} / h, \quad (\text{B.11})$$

where \bar{u} and \bar{v} are the depth-integrated currents. These derived bottom currents were converted to bottom stresses according to Eq. (B.10). Then Eq. (B.9) zonal-average bottom stresses were computed via a simple average of relevant station bottom stress estimates. Station TTE and P bottom stress estimates were averaged to produce *Inner Zone* bottom stresses; and NSA and NSD bottom stresses were averaged for the *Outer Zone*.

The Y-directed lateral stresses at a station on the east- or west-facing lateral wall was estimated from

$$\frac{T_y}{\rho_o} = \frac{\mu_H}{\rho_o} \left(\frac{\partial(V/H)}{\partial x} \right) = v_H \left(\frac{\partial(V/H)}{\partial x} \right) \approx v_H \frac{\delta(V/H)}{\Delta x}, \quad (\text{B.12a})$$

and the X-directed lateral stresses on the north- or south-facing lateral wall is estimated from

$$\frac{T_x}{\rho_o} = \frac{\mu_H}{\rho_o} \left(\frac{\partial(U/H)}{\partial y} \right) \approx v_H \frac{\delta(U/H)}{\Delta y}, \quad (\text{B.12b})$$

where v_H is the commonly used horizontal eddy friction coefficient that we assumed was $5 \text{ m}^2 \text{ s}^{-1}$ after Black et al. (2005).

The zone-average lateral stress terms in Eq. (B.9) were estimated using the following algorithms:

$$\frac{\rho_o}{A} \left\{ \frac{1}{\rho_o} \langle \delta_x HT_y \rangle_y \right\} \approx \frac{\rho_o}{A} \left\{ \frac{v_H}{\Delta x} (h_p - h_{TE}) [(\bar{v}/h)_{TE} - (\bar{v}/h)_P] \Delta y \right\}, \quad (\text{B.13a})$$

$$\frac{\rho_o}{A} \left\{ \frac{1}{\rho_o} \langle \delta_y HT_x \rangle_x \right\} \approx \frac{\rho_o}{A} \left\{ \frac{v_H}{\Delta y} (h_D - h_P) [(\bar{u}/h)_D - (\bar{u}/h)_P] \Delta x \right\}, \quad (\text{B.13b})$$

$$\frac{\rho_o}{A} \left\{ \frac{1}{\rho_o} \langle \delta_x HT_y \rangle_y \right\} \approx \frac{\rho_o}{A} \left\{ \frac{v_H}{\Delta x} (h_A - h_P) [(\bar{v}/h)_A - (\bar{v}/h)_P] \Delta y \right\}, \quad (\text{B.13c})$$

where Eqs. (B.13a) and (B.13b) pertain to the IZ, while Eqs. (B.13b) and (B.13c) pertain to the OZ estimates, respectively.

Appendix C. Vorticity budget term estimation

Given the basic rotary nature of the tidal eddy motion, we view the formation and evolution of the transient tidal eddy motion through the lens of the conservation of zonally averaged vertical transport vorticity equation. The transport vorticity budget used in this study is derived as follows.

The components of the vertically integrated continuity equation is

$$\frac{\partial \eta}{\partial t} + \frac{\partial U}{\partial x} + \frac{\partial V}{\partial y} = 0 \quad \text{or} \quad \frac{\partial H}{\partial t} + \frac{\partial U}{\partial x} + \frac{\partial V}{\partial y} = 0. \quad (\text{C.1})$$

where $\eta(x, y, t)$ is the sea level departure from mean sea level, the volume transports are U and V ; related to which are the depth-averaged velocities $\bar{u} = U/H$; $\bar{v} = V/H$, where the total depth $H(x, y, t) = \eta(x, y, t) + h(x, y)$ in which $h(x, y)$ is the depth distribution relative to mean sea level.

Thus the momentum equations for the horizontal transports U and V respectively are

X-direction

$$\frac{\partial U}{\partial t} + \frac{\partial \bar{u} U}{\partial x} + \frac{\partial \bar{v} U}{\partial y} - fV = -\frac{H}{\rho_o} \frac{\partial p_b}{\partial x} - \frac{\tau_x^b}{\rho_o} + \frac{1}{\rho_o} \left(\frac{\partial HT_x}{\partial y} + \dots \right). \quad (\text{C.2a})$$

Y-direction

$$\frac{\partial V}{\partial t} + \frac{\partial \bar{u} V}{\partial x} + \frac{\partial \bar{v} V}{\partial y} + fU = -\frac{H}{\rho_o} \frac{\partial p_b}{\partial y} - \frac{\tau_y^b}{\rho_o} + \frac{1}{\rho_o} \left(\frac{\partial HT_y}{\partial x} + \dots \right), \quad (\text{C.2b})$$

where we present only the presumed leading terms in the lateral diffusion terms.

Following Park and Wang (2000), the conservation of transport vorticity equation is computed by taking the curl of Eq. (C.2); that is taking $-(\partial[\text{Eq}(C2a)]/\partial y)$ giving

$$-\frac{\partial}{\partial t} \left(\frac{\partial U}{\partial y} \right) - \frac{\partial \bar{u} U}{\partial x \partial y} - \frac{\partial \bar{v} U}{\partial y^2} + f \frac{\partial V}{\partial y} = +\frac{H}{\rho_o} \frac{\partial p_b}{\partial x \partial y} + \frac{1}{\rho_o} \frac{\partial p_b}{\partial x} \frac{\partial H}{\partial y} + \frac{1}{\rho_o} \frac{\partial \tau_x^b}{\partial y} - \frac{1}{\rho_o} \left(\frac{\partial HT_x}{\partial y^2} \right); \quad (\text{C.3a})$$

and taking $(\partial[\text{Eq}(C2b)]/\partial x)$ giving

$$\begin{aligned} \frac{\partial}{\partial t} \left(\frac{\partial V}{\partial x} \right) + \frac{\partial \bar{u} V}{\partial x^2} + \frac{\partial \bar{v} V}{\partial x \partial y} + f \frac{\partial U}{\partial x} \\ = -\frac{H}{\rho_o} \frac{\partial p_b}{\partial x \partial y} - \frac{1}{\rho_o} \frac{\partial p_b}{\partial y} \frac{\partial H}{\partial x} - \frac{1}{\rho_o} \frac{\partial \tau_y^b}{\partial x} + \frac{1}{\rho_o} \left(\frac{\partial HT_y}{\partial x^2} \right) \end{aligned} \quad (\text{C.3b})$$

and adding Eqs. (C.3a) and (C.3b); yielding

$$\begin{aligned} \frac{\partial}{\partial t} \left(\frac{\partial V}{\partial x} - \frac{\partial U}{\partial y} \right) + \left(\frac{\partial \bar{u} V}{\partial x^2} + \frac{\partial \bar{v} V}{\partial x \partial y} - \frac{\partial \bar{u} U}{\partial x \partial y} - \frac{\partial \bar{v} U}{\partial y^2} \right) + f \left(\frac{\partial U}{\partial x} + \frac{\partial V}{\partial y} \right) = \\ + \frac{1}{\rho_o} \frac{\partial p_b}{\partial x} \frac{\partial H}{\partial y} - \frac{1}{\rho_o} \frac{\partial p_b}{\partial y} \frac{\partial H}{\partial x} - \left(\frac{1}{\rho_o} \frac{\partial \tau_y^b}{\partial x} - \frac{1}{\rho_o} \frac{\partial \tau_x^b}{\partial y} \right) - \frac{1}{\rho_o} \left(\frac{\partial^2 HT_x}{\partial y^2} - \frac{\partial^2 HT_y}{\partial x^2} \right). \end{aligned} \quad (\text{C.4})$$

Recalling Eq. (B.5), the bottom stress term in Eq. (C.4) can be rewritten as

$$\begin{aligned} \left(\frac{1}{\rho_o} \frac{\partial \tau_y^b}{\partial x} - \frac{1}{\rho_o} \frac{\partial \tau_x^b}{\partial y} \right) &= \left[\nabla \times C_d \left| \vec{V}^b(x, y) \right| (u^b \vec{i} + v^b \vec{j}) \right] \\ \bullet \vec{k} &= \left[\nabla \times C_d \left| \vec{V}^b(x, y) \right| \vec{V}^b(x, y) \right] \bullet \vec{k} \\ &= C_d \left| \vec{V}^b(x, y) \right| \omega^b - C_d \left(\vec{V}^b(x, y) \times \nabla \left| \vec{V}^b(x, y) \right| \bullet \vec{k} \right). \end{aligned} \quad (\text{C.5})$$

Making use of the hydrostatic relation

$$p_b = \rho_o g \eta$$

and substituting Eq. (C.5) and the continuity equation (C.1) appropriately in to Eq. (C.4) gives

$$\begin{aligned} \frac{\partial \Pi}{\partial t} + \left(\frac{\partial \bar{u} V}{\partial x^2} + \frac{\partial \bar{v} V}{\partial x \partial y} - \frac{\partial \bar{u} U}{\partial x \partial y} - \frac{\partial \bar{v} U}{\partial y^2} \right) = -g \left(\frac{\partial H}{\partial x} \frac{\partial \eta}{\partial y} - \frac{\partial H}{\partial y} \frac{\partial \eta}{\partial x} \right) + f \frac{\partial \eta}{\partial t} \\ - \left[C_d \left| \vec{V}^b \right| \omega^b - C_d \left(\vec{V}^b \times \nabla \left| \vec{V}^b \right| \bullet \vec{k} \right) \right] - \frac{1}{\rho_o} \left(\frac{\partial^2 HT_x}{\partial y^2} - \frac{\partial^2 HT_y}{\partial x^2} \right), \end{aligned} \quad (\text{C.6})$$

where $\Pi = \partial V/\partial x - \partial U/\partial y$ is the transport vorticity.

The study region area average of the horizontally integrated vorticity transport equation (C.5) gives

$$\begin{aligned} \frac{\partial \frac{1}{A} \langle \Pi \rangle}{\partial t} + \frac{1}{A} \left\langle \left(\frac{\partial \bar{u} V}{\partial x^2} + \frac{\partial \bar{v} V}{\partial x \partial y} - \frac{\partial \bar{u} U}{\partial x \partial y} - \frac{\partial \bar{v} U}{\partial y^2} \right) \right\rangle = \\ -\frac{g}{A} \left\langle \frac{\partial H}{\partial x} \frac{\partial \eta}{\partial y} - \frac{\partial H}{\partial y} \frac{\partial \eta}{\partial x} \right\rangle + f \left\langle \frac{\partial \eta}{\partial t} \right\rangle - \frac{1}{A} \left\langle \left[C_d \left| \vec{V}^b \right| \omega^b \right. \right. \\ \left. \left. - C_d \left(\vec{V}^b \times \nabla \left| \vec{V}^b \right| \bullet \vec{k} \right) \right] \right\rangle_{\text{(e1)}} + \frac{1}{A \rho_o} \left\langle \left(\frac{\partial^2 HT_y}{\partial x^2} - \frac{\partial^2 HT_x}{\partial y^2} \right) \right\rangle_{\text{(f2)}}, \end{aligned} \quad (\text{C.7})$$

where the area averaging operator is $\langle \dots \rangle/A \equiv (1/A) \int_{y_1}^{y_2} \int_{x_1}^{x_2} \dots dx dy$, with a domain area of $A = \Delta x \Delta y = (x_2 - x_1)(y_2 - y_1)$ and reference water density of ρ_o .

Physically the local rate change of the transport vorticity production – term (a) in Eq. (C.7) transport vorticity budget – is influenced by mechanisms represented by terms:

- (b) nonlinear advection of transport vorticity;
- (c) topographic transport vorticity tendency;
- (d) sea surface divergence;
- (e) bottom stress-induced transport vorticity production via:
- (e1) bottom drag dissipation;

Table C1

The algorithms used to estimate the terms in the transport vorticity ($\Pi = \partial V/\partial x - \partial U/\partial y$) conservation equation in the *Inner Zone* (IZ) with hindcast 5-constituent tidal time series. In this formulation, $\bar{\dots}$ indicates depth average and the bottom current drag coefficient $C_d = 0.01$ is used exclusively. Subscripts refer to the stations in main text Fig. 8. Constants have units such that the term units are m/s^2 ; with $\Delta x = 15.47 \text{ km } [(\Delta x)^{-1} = 0.6464 \times 10^{-4} \text{ m}^{-1}]$; $\Delta y = 4.17 \text{ km } [(\Delta y)^{-1} = 2.40 \times 10^{-4} \text{ m}^{-1}]$; and the IZ time/space mean total water depth $H_{IZ} = 23 \text{ m}$.

Transport Vorticity Conservation Term	Estimate algorithm
$\partial(1/A) \langle \Pi^{IZ} \rangle / \partial t$ (a) local time rate change	$\cong (\delta/\delta t) \left[(\delta_X^{IZ} V/\Delta x) - (\delta_Y^{IZ} U/\Delta y) \right]$ with $\delta_X^{IZ} V = (V_P - V_{TE})$; $\delta_Y^{IZ} U = (U_D - U_P)$; assuming $\delta_X^{IZ} V$; $\delta_Y^{IZ} U$ are constant on A
$\frac{1}{A} \left\langle \left(\frac{\partial \bar{V}}{\partial x} + \frac{\partial \bar{U}}{\partial y} - \frac{\partial \bar{U}}{\partial x} \bar{y} - \frac{\partial \bar{V}}{\partial y} \bar{x} \right) \right\rangle$ (b) nonlinear advection	$\cong \bar{u}_{IZ} (\partial \Pi_{IZ}/\Delta x) + \bar{v}_{IZ} (\partial \Pi_{IZ}/\Delta y)$; with $(\partial \Pi_{IZ}/\Delta x) = (\Pi_{OZ} - \Pi_{IZ})/\Delta x$; $(\partial \Pi_{IZ}/\Delta y) \sim 0$; assuming Π_{IZ} and Π_{OZ} are constant on IZ and OZ, respectively; and $\bar{u}_{IZ} = 0.5 [(U_D/H_D) + (U_{TE}/H_{TE})]$; $\bar{v}_{IZ} = 0.5 [(V_D/H_D) + (V_{TE}/H_{TE})]$
$-\frac{g}{A} \left\langle \left(\frac{\partial H}{\partial x} \frac{\partial \eta}{\partial y} - \frac{\partial H}{\partial y} \frac{\partial \eta}{\partial x} \right) \right\rangle$ (c) topographic production tendency	$\cong -g \left\{ \delta H / \delta x \Big _{IZ} [(\eta_D - \eta_P)/\Delta y] - \delta H / \delta y \Big _{IZ} [(\eta_P - \eta_{TE})/\Delta x] \right\}$; assuming $(\partial H/\partial x) \dots (\partial H/\partial y)$ are constant on A
$f \partial \eta / \partial t$ (d) surface divergence-induced	$\delta H / \delta x \Big _{IZ} = 0.00098$; $\delta H / \delta y \Big _{IZ} = 0.00200$; $H_{IZ} = 23 \text{ m}$
$(1/A) \langle ((\partial \tau_x^b / \partial y) - (\partial \tau_y^b / \partial x)) \rangle$	$\cong \delta [f \cdot 0.5 (\eta_D + \eta_{TE})] / \delta t$
$-(C_d/A) \langle \vec{V}^b \omega^b \rangle$ (e1) dissipation	$\cong -C_d s p d_{IZ}^b \omega_{IZ}^b$; $\omega_{IZ}^b = \left[(\delta_X^{IZ} v^b / \Delta x) - (\delta_Y^{IZ} u^b / \Delta y) \right]$ with $\vec{V}^b = u^b \vec{i} + v^b \vec{j}$; $\delta_X^{IZ} v^b = (v_P^b - v_{TE}^b)$; $\delta_Y^{IZ} u^b = (u_D^b - u_P^b)$; $\delta_X^{IZ} v^b = (v_P^b - v_{TE}^b)$; $\delta_Y^{IZ} u^b = (u_D^b - u_P^b)$; $s p d_{IZ}^b = 0.5 (\sqrt{u_{TE}^{b2} + v_{TE}^{b2}}) + 0.5 (\sqrt{u_D^{b2} + v_D^{b2}})$
$(C_d/A) \langle (\vec{V}^b \times \nabla \vec{V}^b) \cdot \vec{k} \rangle$ (e2) speed shear torque	$\cong C_d \left\{ u_{IZ}^b \left[(s p d_D^b - s p d_P^b) / \Delta y \right] - v_{IZ}^b \left[(s p d_P^b - s p d_{TE}^b) / \Delta x \right] \right\}$ with $s p d_D^b = (\sqrt{u_D^{b2} + v_D^{b2}})$, $s p d_P^b = (\sqrt{u_P^{b2} + v_P^{b2}})$, $s p d_{TE}^b = (\sqrt{u_{TE}^{b2} + v_{TE}^{b2}})$
$1/A \langle v_H \nabla^2 \Pi_{IZ} \rangle$ (f) diffusion	$\cong v_H \frac{\delta}{\Delta x} [(\Pi_{OZ} - \Pi_{IZ}) / \Delta x] + O(0)$; where $v_H = 10 \text{ cm}^2/\text{s}$

- (e2) bottom current shear; and
- (f) diffusion of transport vorticity.

As with the momentum budget terms, we estimated these terms in the transport vorticity conservation Eq. (C.7) in the *Inner Zone* (IZ) with the appropriate hindcast 5-constituent tidal time series and the algorithms in Table C1.

References

- Barrick, D.E., 1972. First-order theory and analysis of mf/hf/vhf scatter from the sea. *IEEE Transactions on Antennas and Propagation AP-20*, 2–10.
- Barrick, D.E., Evans, M.W., Weber, B.L., 1977. Ocean surface currents mapped by radar. *Science* 198, 138–144.
- Black, K.P., Gay, S.L., 1987. Eddy formation in unsteady flows. *Journal of Geophysical Research* 92, 9514–9522.
- Black, K.P., Oldman, J., Hume, T., 2005. Dynamics of a 3-dimensional, baroclinic, headland eddy. *New Zealand Journal of Marine & Freshwater Research* 39, 91–120.
- Brown, W.S., 1984. A comparison of Georges Bank, Gulf of Maine and New England shelf tidal dynamics. *Journal of Physical Oceanography* 14, 145–167.
- Brown, W.S., Z. Yu, 2006. CODAR Measurement and Model Simulation of Transient Tidal Eddies in the Western Gulf of Maine, University of Massachusetts, Dartmouth – School for Marine Science and Technology Technical Report SMAST 06-0503, pp. 42 http://www.smast.umassd.edu/OCEANOL/reports/CODAR/tidal_eddies_final_rpt_24may06.pdf.
- Brown, W.S., G.M. Marques, S. King, C. Jakubiak, D. Brown, E. Levine, L. Goodman, 2009. Transient Tidal Eddy Project Data Report: Winter 2008–09, University of Massachusetts, Dartmouth – School for Marine Science and Technology SMAST Technical Report 09-0204, pp. 43. http://www.smast.umassd.edu/OCEANOL/reports/TTE/WINTER_0809_DataRPT_13may09.pdf.
- Brown, W.S., G.M. Marques, 2012. Transient Tidal Eddy Motion in the Western Gulf of Maine, University of Massachusetts, Dartmouth – School for Marine Science and Technology Technical Report SMAST 12-0301, pp. 42 <http://www.smast.umassd.edu/OCEANOL/reports/>.
- Crombie, D.D., 1955. Doppler spectrum of sea echo at 13.56 Mc/s. *Nature* 175, 681–682.
- Edwards, K.A., MacCready, P., Moum, J.N., Pawlak, G., Klymark, J.M., Perlin, A., 2004. Form drag and mixing due to tidal flow past a sharp point. *Journal of Physical Oceanography* 34, 1297–1312.
- Geyer, W.R., Signell, R., 1990. Measurements of tidal flow around a headland with a shipboard acoustic Doppler current profiler. *Journal of Geophysical Research* 95, 3189–3197.
- Geyer, W.R., 1993. Three-dimensional flow around headlands. *Journal of Geophysical Research* 98, 955–966.
- Holboke, Monica J., 1998. Variability of the Maine Coastal Current Under Spring Conditions, Ph.D. Dissertation, Thayer School of Engineering, Dartmouth College, pp. 193.
- Kohut, J.T., Glenn, S.M., 2003. Improving HF radar surface current measurements with measured antenna beam patterns. *Journal of Atmospheric and Oceanic Technology* 20, 1303–1316.
- Lynch, D.R., Ip, J.T.C., Naimie, C.E., Werner, F.E., 1996. Comprehensive coastal circulation model with application to the Gulf of Maine. *Continental Shelf Research* 16, 875–906.
- Lynch, D.R., Holboke, M.J., Naimie, C.E., 1997. The Maine coastal current: spring climatological circulation. *Continental Shelf Research* 17, 605–634.
- Marques, G.M., and W.S. Brown, 2009. Project: Transient Tidal Eddies Model Configuration and Sensitivity, SMAST Technical Report SMAST 09-0207, pp. 24 http://www.smast.umassd.edu/OCEANOL/reports/TTE/model_simulation_report_04may_2009.pdf.
- Marques, G.M., W.S. Brown. Tidal eddy motions in the Western Gulf of Maine, part 2: secondary flow, *Continental Shelf Research*, this issue, <http://dx.doi.org/10.1016/j.csr.2012.02.008>.
- McCabe, R.M., MacCready, P., 2006. Form drag due to flow separation at a headland. *Journal of Physical Oceanography* 36, 2136–2152.
- Moody, J., Butzman, B., Beardsley, R.C., Brown, W.S., Boicourt, W., Daifuku, P., Irish, J.D., Mayer, D.A., Mofjeld, H.E., Petrie, B., Ramp, S., Smith, D., Wright, W.R., 1984. *Atlas of Tidal Elevation and Current Observations on the Northeast American Continental Shelf and Slope*. U.S. Geological Survey Bulletin No. 1611, U.S. Government Printing Office, pp. 122.
- Mukai, A., R. Westerink, J. Luettich, D. Mark (2002). Eastcoast 2001, A Tidal Constituent Database for Western North Atlantic, Gulf of Mexico, and Caribbean sea, Technical Report, Coastal and Hydraulics Laboratory, US Army Corps of Engineers <http://www.unc.edu/ims/ccts/tides/tides.htm>.
- Park, M.-J., Wang, D.-P., 2000. Tidal vorticity around a coastal promontory. *Journal of Oceanography* 56, 261–273.
- Pingree, R., Maddock, L., 1980. The effects of bottom friction and Earth's rotation on an island's wake. *Journal of the Marine Biological Association of the United Kingdom* 60, 499–508.
- Pingree, R., 1978. The formation of the Shambles and other banks by tidal stirring of the seas. *Journal of the Marine Biological Association of the United Kingdom* 58, 211–226.
- Shcherbinina, A., Gawarkiewicz, G., 2008. A coastal current in winter: Autonomous underwater vehicle observations of the coastal current east of Cape Cod. *Journal of Geophysical Research* 113 (C07030), 15.
- Signell, R., Geyer, W.R., 1991. Transient eddy formation around headlands. *Journal of Geophysical Research* 96, 2561–2575.
- Stewart, R.H., Joy, J.W., 1974. HF radio measurement of surface currents. *Deep Sea Research* 21, 1039–1049.
- Stokesbury, K., Harris, B., Marino II, M., Nogueria, J., 2004. Estimation of sea scallop abundance using video survey in off-shore U.S. waters. *Journal of Shellfish Research* 23, 33–40.
- Wolanski, E., Asaeda, T., Tanaka, A., Deleersnijder, E., 1996. Three-dimensional island wakes in the field, laboratory experiments and numerical models. *Continental Shelf Research* 16, 1437–1452.